Cell

Resource

A spatially resolved multi-omic single-cell atlas of soybean development

Graphical abstract

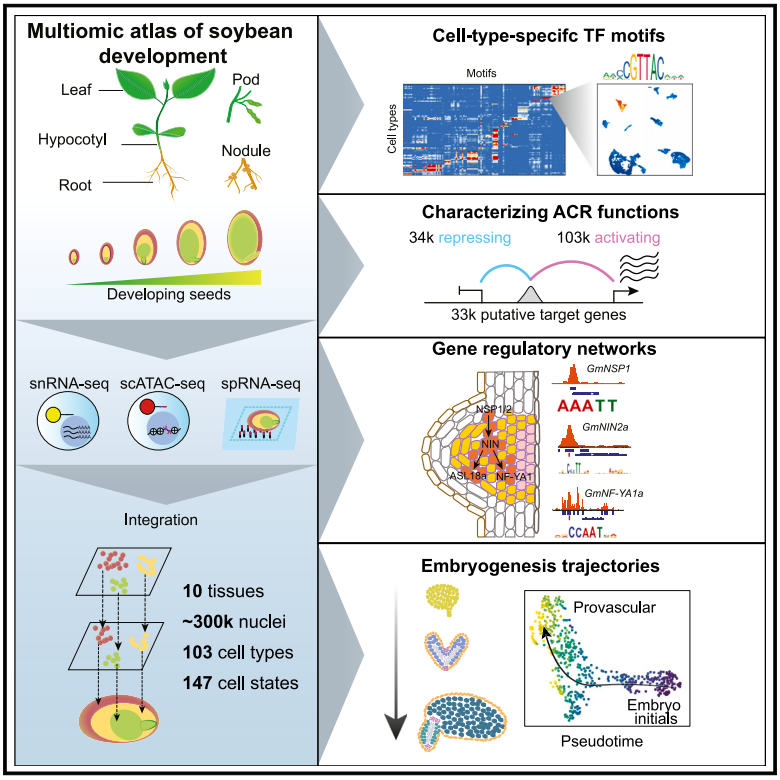

Highlights

- 303,000 accessible chromatin regions (ACRs) identified across 103 distinct cell types
- Identification of cell-type-specific ACRs and transcription factor binding motifs
- Exploration of gene regulatory networks related to symbiotic nitrogen fixation
- Spatially resolved insights into endosperm development and embryonic fate determination

Authors

Xuan Zhang (张旋), Ziliang Luo (罗子良), Alexandre P. Marand, ..., John P. Mendieta, Mark A.A. Minow, Robert J. Schmitz

Correspondence

schmitz@uga.edu

In brief

By integrating spatial transcriptomics and single-cell genomics technologies, we constructed a comprehensive single-cell atlas of gene expression and chromatin accessibility of the crop species *Glycine max* (soybean).

Zhang et al., 2025, Cell *188*, 550–567
January 23, 2025 © 2024 Elsevier Inc. All rights are reserved, including those for text and data mining, AI training, and similar technologies.
https://doi.org/10.1016/j.cell.2024.10.050

CellPress

CellPress

Cell

Resource

A spatially resolved multi-omic single-cell atlas of soybean development

Xuan Zhang (张旋),[1,5] Ziliang Luo (罗子良),[1,5] Alexandre P. Marand,[2,5] Haidong Yan (严海东),[1,4] Hosung Jang,[1] Sohyun Bang,[3] John P. Mendieta,[1] Mark A.A. Minow,[1] and Robert J. Schmitz[1,6,*]

[1]Department of Genetics, University of Georgia, Athens, GA, USA
[2]Department of Molecular, Cellular, and Development Biology, University of Michigan, Ann Arbor, MI, USA
[3]Institute of Bioinformatics, University of Georgia, Athens, GA, USA
[4]Present address: College of Grassland Science and Technology, Sichuan Agricultural University, Chengdu, China
[5]These authors contributed equally
[6]Lead contact
*Correspondence: schmitz@uga.edu
https://doi.org/10.1016/j.cell.2024.10.050

SUMMARY

Cis-regulatory elements (CREs) precisely control spatiotemporal gene expression in cells. Using a spatially resolved single-cell atlas of gene expression with chromatin accessibility across ten soybean tissues, we identified 103 distinct cell types and 303,199 accessible chromatin regions (ACRs). Nearly 40% of the ACRs showed cell-type-specific patterns and were enriched for transcription factor (TF) motifs defining diverse cell identities. We identified *de novo* enriched TF motifs and explored the conservation of gene regulatory networks underpinning legume symbiotic nitrogen fixation. With comprehensive developmental trajectories for endosperm and embryo, we uncovered the functional transition of the three sub-cell types of endosperm, identified 13 sucrose transporters sharing the DNA binding with one finger 11 (DOF11) motif that were co-upregulated in late peripheral endosperm, and identified key embryo cell-type specification regulators during embryogenesis, including a homeobox TF that promotes cotyledon parenchyma identity. This resource provides a valuable foundation for analyzing gene regulatory programs in soybean cell types across tissues and life stages.

INTRODUCTION

Plants are composed of cells derived from various tissues and cellular identities, each containing the same genome but exhibiting highly divergent gene expression that enables specialized functions. One key driver of transcriptional variation is the differential usage of *cis*-regulatory elements (CREs), non-coding loci in the genome that mediate gene expression in a spatiotemporal manner.[1] Spatiotemporal gene expression is controlled by interactions between specific binding motif sequences and cognate transcription factors (TFs), along with cofactors assembled at CREs.[2] Most TFs bind to CREs in nucleosome-depleted accessible chromatin regions (ACRs).[3] Consequently, distinct TF expression and chromatin accessibility patterns establish the gene expression programs of specific cell types. Thus, detailed maps of CRE accessibility and gene expression in diverse cell types are essential for understanding how different cells use the genome, facilitate our functional understanding of the genome, and enable the exploration of gene regulatory networks.

Advancements in single-cell genomics, such as single-nucleus RNA sequencing (snRNA-seq) and single-cell sequencing of assays for transposase-accessible chromatin (scATAC-seq), enable the profiling of transcriptomes and chromatin accessibility from complex tissues at single-cell resolution.[4–6] Extensive single-cell genomic datasets have been generated by large projects in mammals, such as the Human Cell Atlas and the Mouse Cell Atlas.[7–10] In plants, single-cell research has mostly been focused on transcriptomes, often limited to selected organs, tissues, and cell types.[11–17] To date, only three atlas-scale single-cell transcriptomes or chromatin accessibility maps have been reported in *Arabidopsis thaliana*, *Oryza sativa* (rice), and *Zea mays* (maize), each limited to a single modality.[18–20] However, although extremely valuable, these resources are limited by challenges inherent in single-cell genomic technologies, where cells are extracted from their origin in a complex tissue, potentially losing critical biological information and increasing the difficulty of accurate cell-type annotation.[21]

Cell-type annotation is fundamental for elucidating cell population heterogeneity and is typically determined through cell-type markers specifically expressed in one or a few cell types.[12,21] For many non-model species, there are usually insufficient validated marker genes, and cell-type annotation often relies on the expression patterns of the putative orthologs in model plants, mostly *Arabidopsis*.[14,19] However, annotation based on the putative ortholog gene expression can be problematic due to

 © 2024 Elsevier Inc.
All rights are reserved, including those for text and data mining, AI training, and similar technologies.

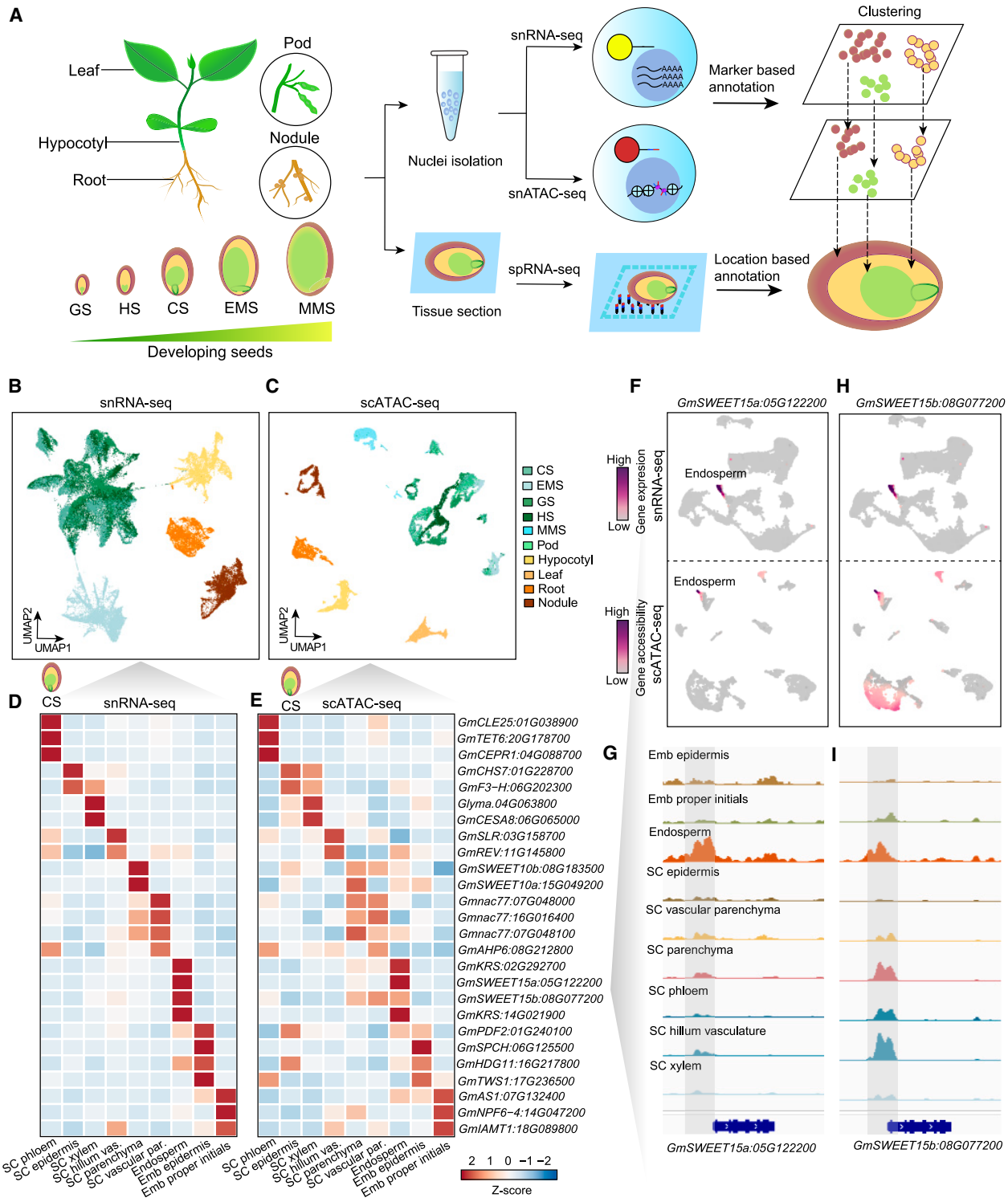

Figure 1. Profiling single-nuclei transcriptomes and chromatin accessibility in soybean

(A) Overview of tissue types and experimental design. Seed stages include globular stage (GS), heart stage (HS), cotyledon stage (CS), early maturation stage (EMS), and middle maturation stage (MMS).

(B and C) Two-dimensional embeddings using uniform manifold approximation and projection (UMAP) depicting similarity among nuclei based on gene expression (B) and gene chromatin accessibility (C). 2,000 nuclei were randomly selected from each tissue and colored by tissue type.

(legend continued on next page)

gene loss, gene duplication, or gene functional diversification following whole-genome duplications. Recently, spatial transcriptomics has provided the opportunity to investigate gene expression profiles within the spatial context of cells, successfully assisting cell-type annotations in animals and plants without needing *a priori* cell-type markers.[22–24] To date, no comprehensive cell-type-level atlas has been completed for any plant, which spans gene expression, ACRs, and spatially resolved cell-type annotations.

Here, we describe a spatially resolved, multimodal single-cell atlas for the crop species *Glycine max* (soybean), which experienced genome duplications approximately 59 and 13 million years ago, resulting in a highly duplicated genome with nearly 75% of its genes present in multiple copies.[25] We measured chromatin accessibility and gene expression in 316,358 nuclei across ten soybean tissues, which identified and characterized 303,199 ACRs in 103 distinct cell types. We found that nearly 40% of ACRs showed cell-type-specific patterns and were enriched for TF binding motifs controlling cell-type specification and maintenance. Focusing on a specific feature of soybean biology, the infected cells that make up the developing nodules, we identified the non-cell autonomous activity of NIN-LIKE PROTEIN 7 (NLP7) and the conservation of a *NIN* gene regulatory network for legume symbiotic nitrogen fixation. Three sub-cell types of endosperm were characterized in detail, revealing a group of 13 sucrose transporters, including two SUGARS WILL EVENTUALLY BE EXPORTED TRANSPORTERs (SWEETs): *GmSWEET15a* and *GmSWEET10a*, which were co-upregulated in late peripheral endosperm, both sharing the DNA binding with one finger 11 (DOF11) binding motif. We also constructed comprehensive developmental trajectories across embryogenesis and early maturation and identified key embryo cell-type specification regulators during embryogenesis. Finally, we created an interactive web atlas to disseminate these resources, which we named the soybean multi-omic atlas (https://soybean-atlas.com/).

RESULTS

Assembly of a single-cell accessible chromatin and expression atlas in soybean

To generate a comprehensive, accessible chromatin and transcriptome atlas across soybean cell types, we collected samples from ten tissues at different stages of the soybean life cycle. These tissues included leaf, hypocotyl, root, nodule, young pod, and five stages of developing seeds: globular stage (GS), heart stage (HS), cotyledon stage (CS), early maturation stage (EMS), and middle maturation stage (MMS; STAR Methods). For each tissue, we conducted scATAC-seq and snRNA-seq with at least two biological replicates, using optimized soybean nuclei isolation methods (Figure 1A; STAR Methods). After filtering low-quality nuclei and doublets, we obtained high-quality accessible chromatin profiles for ten tissues, totaling 200,732 nuclei with a median of 17,755 Tn5 transposase (Tn5) integrations per nucleus, and transcriptome profiles for seven tissues, totaling 115,626 nuclei with a median of 2,474 unique molecular identifiers (UMIs) and 1,986 genes detected per nucleus (Figures S1A–S1H; Table S1). Initial clustering of 2,000 random nuclei from each tissue revealed similar cluster structures in both scATAC-seq and scRNA-seq, with seed tissue nuclei clearly separated from non-seed tissues (Figures 1B and 1C). To further explore cell-type heterogeneity in soybean tissues, we used the *Seurat*[26] and *Socrates*[19] workflows for independent analysis of each tissue. We identified 147 and 97 scATAC-seq and snRNA-seq clusters, respectively, with consistent nuclei proportions in each cluster across replicates (Figures S1I and S1J; Table S1). The scATAC-seq yielded a higher number of clusters compared with scRNA-seq, likely because it captures a broader spectrum of regulatory features, such as chromatin accessibility and potential cell states, enabling finer distinctions between cell populations. These results indicate that our dataset is of high quality and effectively captures the diversity of cell types and states in soybean (Table S1).

To annotate cell clusters, we collected a set of marker genes from the literature spanning multiple species, including soybean, *Arabidopsis*, and maize, and matched them to expected soybean cell types. Cell types were assigned based on a manual review of marker gene performance and evaluation of enriched biological processes (STAR Methods, Table S2). For example, in CS seeds, we identified 17 clusters in scATAC-seq and 18 clusters in snRNA-seq, with high concordance between the two replicates (Figures S1K and S1L). By comparing the single-cell data with previously published laser-capture microdissection RNA-seq datasets,[27,28] we identified the three main regions of soybean seeds: seed coat, endosperm, and embryo, as well as specific cell types, such as the seed coat endothelium and seed coat inner integument (Figures S1M and S1N). Additional cell types were annotated based on representative marker genes (Figures 1D and 1E). For instance, the plasma membrane sugar transporter GmSWEET15, which mediates sucrose export from the endosperm to the embryo[29] and has paralogous genes from a whole-genome duplication, *GmSWEET15a* and *GmSWEET15b*, showed enriched expression and chromatin accessibility in the endosperm. This was accompanied by neighboring ACRs with high sequence similarity (86.95% identical matches) between the two genes, suggesting conservation of CREs responsible for the endosperm-specific expression of these genes (Figures 1F–1I). After comprehensive annotation and subsequent analysis, we identified a total of 103 and 79 cell types in the scATAC-seq and snRNA-seq data, respectively, with a high correlation between gene accessibility from scATAC-seq and gene expression from snRNA-seq for the same cell

(D and E) *Z* score heatmap of gene expression (D) and gene chromatin accessibility (E) for representative marker genes across shared cell types in soybean CS seeds. SC, seed coat; Emb, embryo.
(F and G) UMAP embeddings overlaid with gene expression (top) or gene accessibility (bottom) (F) and pseudobulk cell-type Tn5 integration site coverage (G) around the endoderm marker gene *GmSWEET15a*.
(H and I) Similar to (F and G), but for the paralog gene *GmSWEET15b*.
See also Figures S1, S2, and S3 and Tables S1 and S2.

types (Figures S2 and S3; Tables S1 and S2). Notably, dividing cells were absent across all scATAC-seq datasets but were clearly annotated in most snRNA-seq datasets (Figures S2M–S2P; Table S1). This aligns with previous reports indicating that cell cycle gene-related heterogeneity is more easily detected at the transcriptional level than through chromatin accessibility in humans.[30]

Validation of cell-type identity with spatial transcriptomics

The limited availability of experimentally validated marker genes for cell-type annotation in scATAC-seq and scRNA-seq datasets is a common challenge, particularly in non-model species, as homology-based marker identification is problematic due to gene loss, duplication, or neofunctionalization. To validate the cell-type annotations for the single-cell datasets, we conducted spatial RNA-seq (spRNA-seq) for five tissue types, all at the same developmental stages as the single-cell datasets (root, hypocotyl, seed at HS, CS, and EMS). Multiple serial tissue sections were placed on a 10× Genomics Visium spatial slide (Figures 2A and S4A). In total, we profiled 12,490 high-quality spatial spots across these tissues. The median gene number per spot ranged from 453 to 6,262 across all tissue types.

Unsupervised clustering of the expression profiles revealed that spatial spot clusters showed cell-type-specific spatial localization (Figures 2B and S4B). For example, we identified 13 clusters in the CS seed dataset (Figure 2B). Four of these clusters are localized in the embryo region, three in the endosperm region, and six within the seed coat region (Figure 2B). This indicates high-quality spatial transcriptome data and enables accurate cell-type annotation based on tissue histology. The Visium spatial slides are designed with 55-μm resolution spots, which often capture gene expression profiles from multiple cells. To study the spatial expression profile at single-cell resolution and validate the snRNA-seq cell-type annotation, we performed deconvolution analysis using spRNA-seq and snRNA-seq datasets of the same tissue types. A prediction score of each snRNA-seq cell was calculated to quantify the certainty of the association between snRNA-seq cells and their predicted spatial spots. We observed high prediction scores between similar cell types that were independently annotated in the two datasets (Figures 2C and S4C), supporting a robust annotation.

Leveraging the spatial transcriptome data, we corroborated known marker genes selected for the snRNA-seq cell-type annotation (Figure 2D; Table S2). For example, *GmKTi3* (*Glyma.08G341500*), Gm*PLETHORA2* (Gm*PLT2, Glyma.12G056300*), *GmSWEET15a (Glyma05G12200)*, and *GmSWEET10b* (*Glyma.08G183500*) are known to be exclusively transcribed to the soybean embryo,[31] *Arabidopsis* root apical meristem (RAM),[32] CS endosperm,[29] and seed coat parenchyma,[33] respectively. Our spRNA-seq data showed highly specific expression patterns consistent with these prior observations, providing a valuable tool for *in situ* marker validation.

To identify soybean cell-type-specific markers, we performed *de novo* marker identification using the spRNA-seq and snRNA-seq datasets (Figures 2E and 2F; Table S2). With the *de novo* markers from spRNA-seq, we distinguished similar cell types that are spatially differentiated. For example, we identified three subclusters of endosperm cells and annotated them as micropylar, peripheral, and chalazal endosperm based on their localization in the seed (Figure 2F). The spatial *de novo* markers from these cell types showed distinct expression patterns in the corresponding snRNA-seq and scATAC-seq subclusters. By integrating the single-cell datasets with spRNA-seq, we not only validated cell-type annotations but also resolved spatially differentiated sub-cell types.

Identification and characterization of ACR diversity across cell types

To identify ACRs across the 103 cell types, we aggregated chromatin accessibility profiles from all nuclei within each cell cluster and applied a peak calling procedure optimized for single-cell data (STAR Methods). This uncovered 303,199 non-overlapping ACRs, ranging from 137,046 to 193,792 per tissue (Figure 3A). Compared with bulk ATAC-seq from leaf at the same stage (STAR Methods), scATAC-seq identified almost twice as many ACRs despite having fewer total reads, with many cell-type-specific ACRs (ctACRs) masked by bulk tissue profiling (Figures 3B and 3C). Next, we categorized ACRs based on their proximity to annotated genes: 128,916 (45.52%) overlapped genes (genic ACRs), 74,655 (24.62%) were within 2 kilobases (kb) of genes (proximal ACRs), and 99,628 (32.86%) were more than 2 kb away from genes (distal ACRs). Distal ACRs had significantly higher cell-type specificity than genic and proximal ACRs, suggesting an important role in establishing cell-type-specific gene expression patterns (t test, p value $< 2.2e{-}16$, Figure S5A). Furthermore, genetic diversity from the soybean haplotype map (GmHapMap)[34] was remarkably reduced, and TF motifs were enriched at the summit of all three groups of ACRs, supporting the functionality of the identified ACRs (Figures 3E and S5B).

ACRs can be generally classified as activating or repressive, either positively or negatively regulating gene expression, respectively.[35] To predict ACR function, we associated ACRs with putative target genes based on the correlation between ACR accessibility and nearby gene expression across all cell types (Figure 3F, STAR Methods). This approach identified 145,638 ACR-gene associations for 137,245 ACRs and 33,068 genes, with an average of four ACRs per gene (Figure 3G; Table S3). We found that cell-type specificity of gene expression was positively correlated with the number of associated ACRs, suggesting that increased regulatory complexity is a generalizable feature of restricted gene expression patterns (Figure 3H). Next, we categorized ACRs with positive correlations as activating ACRs and those with negative correlation as repressive ACRs (Figures 3I, 3L, 3M, S5C, and S5D). Overall, 71.9% were activating, 24.1% were repressive, and 3.9% had ambiguous functions with mixed significant positive and negative correlations with flanking genes (Figure 3J). Activating ACRs were more likely to act proximally compared with repressive ACRs (Figure 3K). Notably, we identified three known activating CREs (Figures 3N–3P), including positive regulation of *Glyma.03g229700* in seed tissues,[36] *ASYMMETRIC LEAVES2-LIKE 18 (ASL18)*, a known root nodule symbiosis marker,[37] and a pod shattering-resistance-related gene.[38] To evaluate the effects of whole-genome duplication on ACR activity, we compared ACR-gene correlations for duplicated regulatory

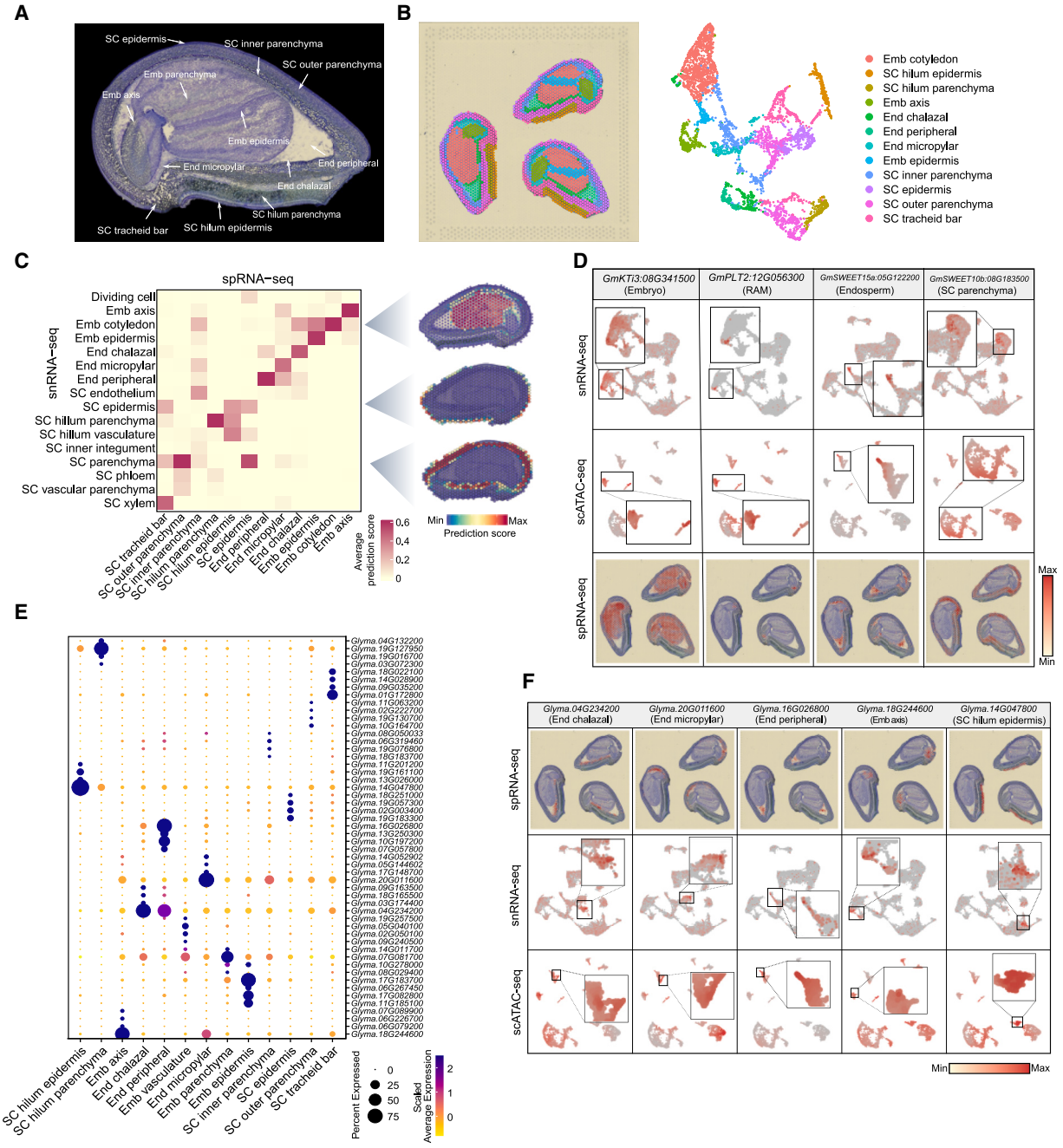

Figure 2. A spatially resolved transcriptome facilitates cell-type annotation for soybean seeds

(A) The histological structure of soybean seeds at the CS.

(B) The visualization of spatial spot clusters on the tissue section (left) and on the UMAP plot (right).

(C) Heatmap of the snRNA-seq cell-type prediction scores on the spRNA-seq cell types (left) and the spatial distribution of predicted snRNA-seq cell types on the tissue section (right).

(D) The validation of known marker genes used in the scRNA-seq data. The gene expression of selected markers was plotted on the UMAP of snRNA-seq data (top), scATAC-seq data (middle), and on the spatial plot of the tissue section (bottom).

(E) Dot plot of the top *de novo* marker genes identified for each cell type in the spRNA-seq data.

(F) The validation of spatial *de novo* marker genes in the single-cell data. The gene expression of selected markers was plotted on the spatial plot of the tissue section (top), the UMAP of snRNA-seq data (middle), and the scATAC-seq data (bottom).

See also Figure S4 and Tables S1 and S2.

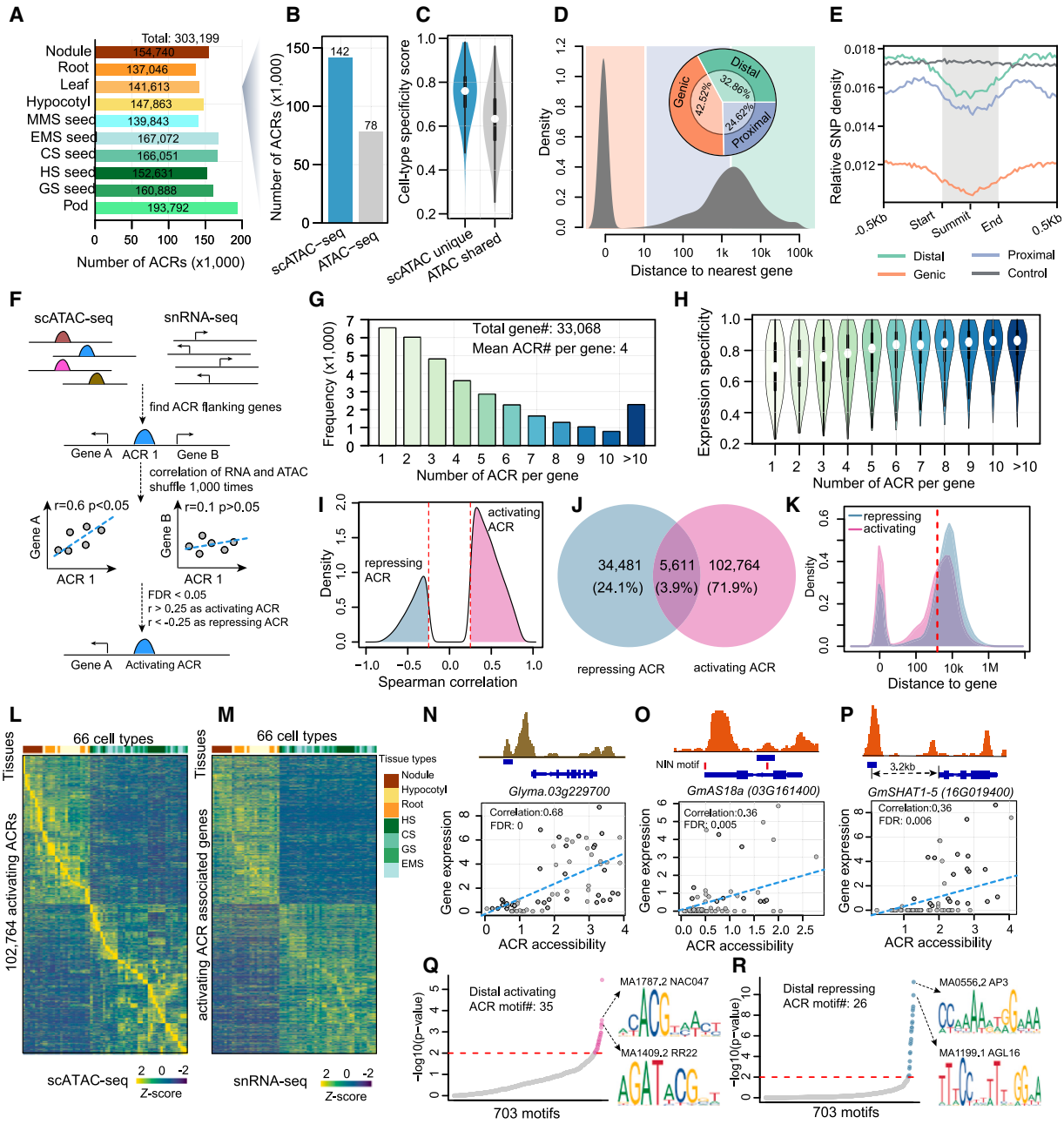

Figure 3. Characterization of ACRs across cell types

(A) Number of ACRs identified in each tissue.

(B) Comparison of the number of ACRs identified using scATAC-seq versus bulk ATAC-seq in leaf tissues.

(C) Distribution of cell-type specificity score for ACRs shared between bulk ATAC and scATAC and those specific to scATAC-seq.

(D) Bimodal distribution of ACR distances to the nearest gene. ACRs are categorized into three groups based on the distance from the summit to the nearest gene: genic ACRs (overlapping or within 10 bp of genes), proximal ACRs (within 2 kb of genes), and distal ACRs (more than 2 kb away from genes).

(E) Relative SNP density within 500-bp flanking regions of different classes of ACRs and control regions.

(F) Schematic overview of the computational strategy used to predict the activity function of ACRs.

(G) Distribution of genes associated with different numbers of ACRs.

(H) Distribution of expression specificity for genes associated with different numbers of ACRs.

(I) Density distribution of the overall Spearman's correlation coefficient between ACRs and flanking genes. The red line indicates the minimum correlation cutoff at 0.25 or −0.25.

(J) Venn diagram analysis of activating and repressing ACRs.

(legend continued on next page)

regions. We found that most duplicated ACR-gene pairs exhibit similar correlations between chromatin accessibility and gene expression (90% coincidence), with most ACR-gene pairs positively correlated (79% of pairs; Figures S5E–S5G). These results suggest a high level of functional conservation among duplicated ACRs. To identify motifs that could act as distal activators or repressors, we conducted a TF motif enrichment analysis on the distal activating and repressing ACRs. We found 35 motifs enriched in distal activating ACRs, and six of the top ten motifs had known transcriptional activator activity, such as NAC DOMAIN CONTAINING PROTEIN 47 (NAC047)[39] and RESPONSE REGULATOR 22 (RR22)[40] (Figure 3Q; Table S3). Additionally, 26 motifs were enriched in distal repressive ACRs, primarily type II MADS-box factors (MCM1, AGAMOUS, DEFICIENS, and SRF) like APETALA3 (AP3)[41] and AGAMOUS-LIKE 16 (AGL16),[42] known transcriptional repressors involved in floral organ specification (Figure 3R; Table S3). Type II classic MADS-box genes are key developmental regulators in angiosperms and are well-studied due to their role in floral organ specification.[43] We observed distinct MADS gene expression patterns in seed versus non-seed tissues, consistent with MADS-box genes regulating reproductive growth by transcriptionally repressing distal genes. These results provide a foundation for dissecting gene regulatory programs at cell-type resolution.

Identification and characterization of ctACRs

This single-cell atlas provides an excellent opportunity to characterize the heterogeneous regulatory programs underlying specialized cell-type functions. To this end, we identified ctACRs that were significantly more accessible in only one or two cell types within each tissue (STAR Methods). Approximately 40.23% of the ACRs (122,558 ACRs) were identified as ctACRs across ten tissues, ranging from 12,711 in root to 37,897 in young pod (Figure 4A; Table S4). As expected, ctACRs are associated with greater gene expression specificity (Figure S5H). We observed a higher number of ctACRs in seed-related tissues compared with non-seed tissues, with a higher number of endosperm-specific ACRs in young developing seeds compared with the other cell types (Figure S5I). Highly dynamic chromatin accessibility in seed endosperm has also been observed in rice,[20] suggesting that complex regulatory dynamics in endosperm may be conserved in plants. To investigate this further, we evaluated DNA cytosine methylation across all sequence contexts.[44] We found endosperm-specific ACRs were demethylated compared with leaf tissue (Figure S5J), indicating that the increased number of ACRs in the endosperm corresponds with genome-wide hypomethylation in the endosperm. Although the proportion of ACRs located in proximal regions was similar across ctACRs and non-ctACRs, we observed a higher proportion of distal ACRs among ctACRs (Figure S5K), showcasing the importance of distal ACRs in contributing to cell-type-specific gene regulation. Moreover, we found ctACRs had a lower density of single-nucleotide polymorphisms compared with non-ctACRs, implicating positive selection of ctACRs in soybean breeding (Figure S5L).

Transposable elements (TEs) contribute to cell-type-specific CREs in both mammals and plants.[19,45,46] For example, cell-type-specific enhancers are often found within long terminal repeat retrotransposons (LTRs) in maize.[19] In soybean, a similar proportion of ctACRs and non-ctACRs overlapped with TEs (Figure 4B). However, TE enrichment analysis indicated significant enrichment of hAT TIR transposons overlapping ctACRs, distinct from maize (Figure 4B; Fisher's exact test, false discovery rate (FDR) < 10e−16). To investigate the role of TEs and their relationship to ctACRs, we conducted an enrichment analysis comparing TEs overlapping ctACRs and non-ctACRs for each cell type. We found significant TE enrichment in nine cell types largely corresponding to the endosperm across seed development stages (Fisher's exact test, FDR < 0.01; Figure 4C), with 579 (59%) of these endosperm-specific ACRs present at two or more developmental stages (Figure S5M). Similar to the methylation pattern observed in all endosperm-specific ACR, those overlapping hAT TIR transposons were also demethylated compared with leaf tissue (Figure S5J), and ctACRs were largely enriched in the 5′ and 3′ regions of hAT TIR transposons (Figure S5N). Taken together, these data suggest that demethylation of hAT TIR transposons in seed endosperm unlocks a major source of regulatory activity in soybean.

Identification of key TF regulators that define distinct cell identities

Identifying the TFs involved in establishing and maintaining diverse cell identities is a central goal in developmental biology. We leveraged these data to systematically assess which TF motifs are enriched in ctACRs across tissues, thus identifying key regulatory networks potentially critical in cell fate specification.

Toward this goal, we identified overrepresented TF motifs from the JASPAR database[47] in ctACRs relative to non-ctACRs across cell types within each tissue, revealing both known and unknown potential regulators (Figures 4D and S5O; Table S4). For example, the HOMEODOMAIN GLABROUS 11 (HDG11) motif (MA0990.2), an established regulator of epidermal cell,[48] is highly accessible in epidermal cells of hypocotyl, root, leaf, and CS seeds. Similarly, the DOF1.6 motif (MA1275.1) is enriched in procambium-related cells across all tissues (Figure S5P; Table S4), whereas the known endosperm-specific transcriptional activator,[49] MYB118 (MYELOBLASTOSIS 118), motif is enriched for cell-type-specific chromatin accessibility in endosperm and is specifically expressed in soybean endosperm cells

(K) Density distribution of the distance between the pair of ACRs and genes for the activating and repressing ACRs. The red line indicates the distal association cutoff at 2 kb.
(L and M) Heatmap showing chromatin accessibility of activating ACR (L) and the expression of associated genes (M).
(N–P) Pseudobulk cell-type Tn5 integration site coverage patterns around gene bodies (top) and scatter plots of ACR accessibility and gene expression across 66 cell types (bottom) for *Glyma.03g229700*, *GmAS18a (03G161400)*, and *GmSHAT1-5 (16G019400)*, respectively.
(Q and R) TF motif enrichment of distal activating ACRs (Q) and distal repressing ACRs (R).
See also Figure S5 and Table S3.

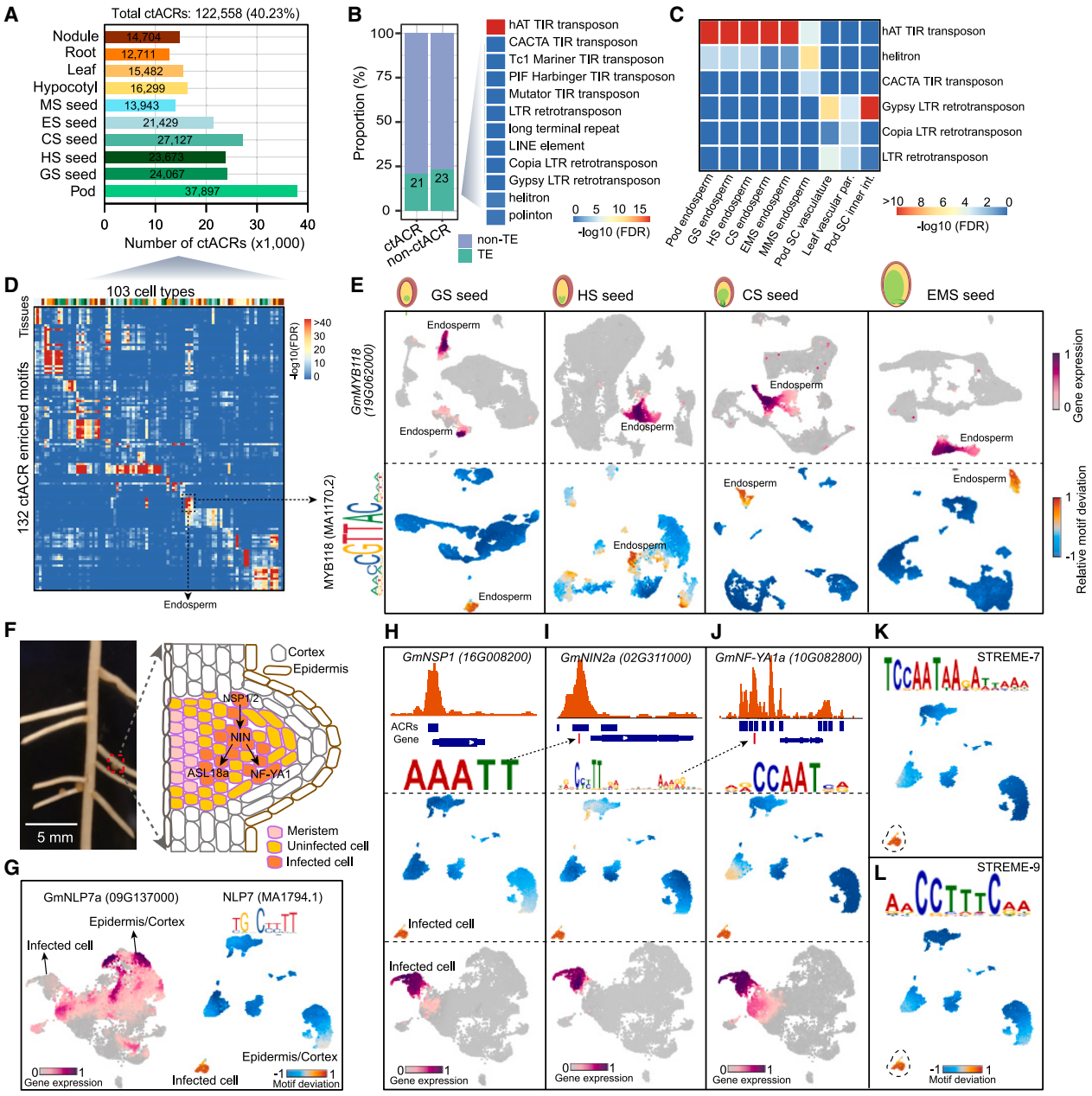

Figure 4. Characterization of cell-type-specific ACRs, motif, and TFs

(A) Number of ctACRs identified in each tissue.

(B) Proportion of ACRs that overlap with TEs and TE enrichment in all ctACRs.

(C) TE enrichment in ctACRs for each cell type.

(D) Heatmap of TF motif enrichment across 103 cell types.

(E) UMAP embeddings overlaid with gene expression of *GmMYB118* (top row) or TF motif deviation score of the MYB118 binding motif (bottom row) across four developmental stages of seeds.

(F) Image of a root with nodules (left) and an illustration of major cell types and the gene regulatory pathway in infected cells of developing nodules.

(G) UMAP embeddings overlaid with gene expression of *GmNLP7a* and TF motif deviation score of NLP7 in nodule tissue.

(H–J) Pseudobulk cell-type Tn5 integration site coverage pattern around gene body (top), UMAP embedding overlaid motif deviation score (middle), and gene expression (bottom) for *GmNSP1*(H), *GmNIN2a* (I), and *GmNF-YA1a* (J). The dotted arrow indicates the TF motif binding site.

(K and L) UMAP embedding overlaid TF motif deviation score for *de novo* motifs of STREME-7 and STREME-9.

See also Figure S5 and Table S4.

across four developmental stages (Figure 4E). Thus, our integrated atlas faithfully recapitulates known regulatory dynamics underlying diverse cell states.

Adapting these analyses, we aimed to characterize the regulatory signatures of developing nodules, where symbiosis between legumes and soil bacteria fixes nitrogen for both the plant and the natural or agricultural ecosystem.[50] Nitrogen fixation occurs in infected cells, a specific cell type that encapsulates the nitrogen-fixing bacteria (Figure 4F). However, how these cells are altered in terms of their CRE usage after infection remains underexplored. We found a series of symbiotic nitrogen fixation genes that were specifically expressed and accessible in infected cells (Figures S2C and S2D). We found a total of 73 TF motifs enriched in infected cells, including the binding motif of NLP7, a known regulator of root nodule symbiosis[51,52] (Figure 4G; Table S4). Notably, there was a spatial discordance between *NLP7*'s expression in epidermis or cortex and the global chromatin of its binding site in infected cells, suggesting non-cell autonomous activity[19] (Figure 4G). The top two most enriched TF motifs in infected-cell-specific ACRs were AHL13 (MA2374.1), which regulates jasmonic acid biosynthesis and signaling,[53] and ANTHOCYANINLESS 2 (MA1375.2), which regulates anthocyanin accumulation and primary root organization[54] (Figures S5Q and S5R).

Only seven of the motifs in the JASPAR database[47] are from soybean, with most being from *Arabidopsis* (580) or other species (218), potentially limiting the study of important soybean TFs. For example, key regulator genes essential for initiating cortical cell divisions and microbial infection during nodulation, such as NODULATION SIGNALING PATHWAY 1 (NSP1),[37] NODULE INCEPTION (NIN),[37] ASYMMETRIC LEAVES 2-LIKE 18 (ASL18),[37] and nuclear factor-YA1 (NF-YA1),[50] were highly expressed in infected cells yet lack representation in the JASPAR database (Figures 4H–4J). Leveraging the predicted motifs of these TFs from studies in *Medicago truncatula* and *Lotus* japonicus,[50] we found strong TF motif enrichment within infected cell ACRs, corroborating their conservation in soybean (Figures 4H–4J; Table S4).

To comprehensively identify potential TF binding motifs in infected cells, we performed *de novo* motif enrichment in infected-cell-specific ACRs, identifying 10 enriched motif clusters (Table S4). Interestingly, all four binding motifs of known key regulators (NLP7, NIN, NSP1, and NF-YA1) matched a *de novo* motif (Figure S5S). Additional TF motifs matched known motifs in the JASPAR database, including binding sites for AP2/ERFs, B3 domain-containing TFs, RAV2, basic leucine zipper (bZIP) TFs, ethylene-responsive (ERF) TFs, and protein BASIC PENTACYSTEINE1 (BPC1) TFs (Figure S5T). Notably, among these motifs, the GCC-box motif is a known pathogenesis-related promoter element that recruits ERF TFs, including the ethylene response factor required for nodulation1 (ERN1), which is essential for infection-thread formation and nodule organogenesis in *Medicago*.[55] We also identified two unknown motifs, which are specifically accessible in the infected cell, including the AACC TTTCAA motif (STREME-7) and the TCCAATAAGATTAAA motif (STREME-9) (Figures 4K and 4L), implicating potential regulators of nodule development and potential targets for soybean improvement. In summary, integrating TF motif enrichment with snRNA-seq enabled the identification of known and *de novo* TF binding motifs of key regulators essential for cell-type specification.

Characterizing three sub-cell types of endosperm across seed development

The endosperm plays a crucial role in supporting embryo growth by supplying nutrients and other factors during seed development.[56–58] Soybean endosperm is a membrane-like, semi-transparent tissue between the embryo and seed coat. Primary endosperm can be divided into three sub-cell types: micropylar, nearest to the young embryo; peripheral, in the center of the endosperm region; and chalazal, at the opposite end of the embryonic axis toward the seed coat attachment point (Figure 5A).[59] Although the development of these subregions has been well-characterized morphologically, little is known about the molecular processes occurring in these subregions or how their development is coordinated within the context of seed maturation.

By integrating snRNA-seq and spRNA-seq, we separated the three sub-cell types of endosperm (Figure 2B) and gained insights into the cellular processes within each sub-cell type by identifying significantly overrepresented Gene Ontology (GO) terms (p value < 0.01, Figure 5A). Overrepresented GO terms were consistent with the known roles of these endosperm sub-cell types in seed development. For example, the peripheral endosperm is enriched in photosynthesis-related pathways, consistent with the presence of chloroplasts,[59,60] the chalazal endosperm is enriched in vascular transport pathways, aligning with its role in loading maternal resources into developing seeds,[58,61] and the micropylar endosperm is enriched in cutin biosynthetic process pathways, suggesting involvement in cuticle synthesis in the nearby embryo epidermis.[56,57,62]

To define the molecular signatures of endosperm development, we analyzed all endosperm nuclei across four stages (globular, heart, cotyledon, and early maturation) of seed development, integrating scATAC-seq and snRNA-seq modalities (Figures 5B, 5C, and S6A; STAR Methods). Using *de novo* markers from spRNA-seq, we were able to clearly separate and annotate the three sub-cell types (Figure S6B; Table S1). Comparing the proportion of nuclei in each stage across sub-cell types revealed a developmentally associated gain in cell proportion for peripheral and micropylar endosperm but not for chalazal endosperm (Figures S6C–S6H). This observation is consistent with the cellularization of peripheral and micropylar endosperm following nuclei proliferation, whereas the chalazal endosperm undergoes degradation without a clear cellularization process.[59,61]

To better understand chromatin and gene expression dynamics during endosperm development, we performed pseudotime analysis for micropylar and peripheral endosperm using snRNA-seq nuclei as a reference (Figures 5D and 5E). We found that pseudotime was highly correlated with developmental staging, consistent with a biologically rooted cell ordering (Figures 5F and 5G). We then classified genes based on temporal expression patterns across pseudotime into three groups (early, middle, and late) for micropylar and peripheral endosperm (Figures 5H and 5I; Table S5). Consistent with previous observations, GO enrichment analysis captured nuclei proliferation in the early stage and

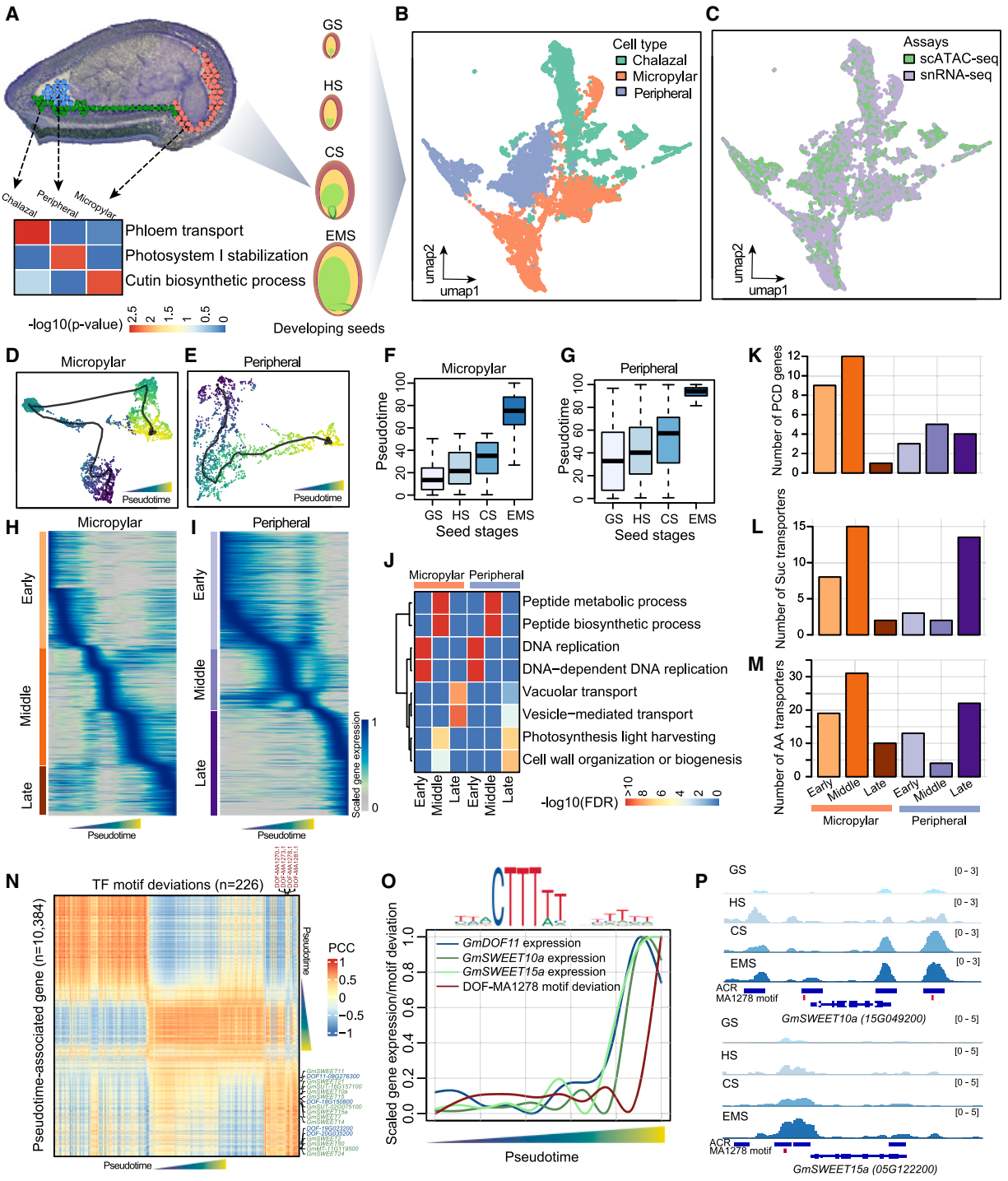

Figure 5. Characterizing three endosperm sub-cell types across seed development

(A) Spatial tissue section showing the three sub-cell types (chalazal, peripheral, and micropylar endosperm) (top) and a heatmap of their representative enriched biological processes (bottom).

(B and C) UMAP embeddings overlaid with cell type (B) or assays (C).

(D and E) UMAP embeddings depicting pseudotime trajectories for micropylar endosperm (D) and peripheral endosperm (E).

(F and G) Comparison of pseudotime and categorical seed stages for micropylar endosperm (F) and peripheral endosperm (G).

(H and I) Heatmap of pseudotime-associated genes (FDR < 0.05) for micropylar endosperm (H) and peripheral endosperm (I).

(J) Heatmap of representative enriched biological processes across pseudotime-inferred stages and cell types.

(K–M) Number of programmed cell death genes (K), sucrose transporters (L), and amino acid transporters (M) across pseudotime-inferred stages and cell types.

(legend continued on next page)

cellularization and functional specification in later stages (Figure 5J). These results indicate robust developmental trajectories for micropylar and peripheral endosperm, allowing high-resolution exploration of the gene regulatory networks underlying cell identity transitions.

During soybean seed development, endosperm cells undergo programmed cell death (PCD) and transfer nutrients to support rapid embryo growth and expansion.[58,63,64] The molecular regulation of endosperm PCD and which nutrient transporters are involved remains poorly understood. By examining mRNA expression patterns of PCD-related genes[65] and sucrose or amino acid transporter genes[66] in developmental trajectories, we found more PCD-related and nutrient transporter genes expressed in early and middle stages of micropylar endosperm than the late stage (Figures 5K–5M; Table S5). The micropylar endosperm, being closest to the embryo, undergoes PCD and serves as an important nutrient source during early seed development.[63] More nutrient transporter genes were expressed in the peripheral endosperm in the late stage, suggesting their role in transferring maternal nutrients in later embryo development.

Sucrose is the major photosynthetic product transported into seeds,[67] and sugar transporters essential for embryo development have been identified and characterized in different plants.[68] We identified a cluster of 13 sugar transporters highly upregulated in the late stage of peripheral endosperm development, including *GmSWEET10a* and *GmSWEET15a*, known to control soybean seed size and oil content.[29,33] As these sugar transporters share similar expression patterns along development, we hypothesized they might share similar gene regulatory structure. To predict shared upstream regulators controlling the 13 sucrose transporters, we scanned all TF motifs in their proximal and genic ACRs and found five motifs from three TF superfamilies shared by all ACRs (Figures S6I–S6K): DOF family, homeodomain-leucine zipper (HD-Zip) TFs, and C2H2 zinc-finger TFs, including INDETERMINATE DOMAIN (IDD) TFs. To determine TF activity dynamics along the peripheral endosperm trajectory, we imputed TF motif deviations from scATAC-seq onto snRNA-seq nuclei, revealing 226 TF motifs with dynamic chromatin accessibility patterns, of which two DOF motifs were highly correlated with the 13 sugar transporter genes (Figures 5N and S6I–S6K). We identified four DOF genes highly expressed in the late stage of peripheral endosperm, including *GmDOF11a* (*Glyma.08G276300*), whose paralog *GmDOF11b* (*Glyma.13G329000*) has been previously implicated in controlling soybean seed size and oil content.[69] Interestingly, *GmSWEET10a* and *GmSWEET15a* were highly expressed in the late stage, and their ACRs harbored the DOF motif (MA1278), which became more accessible throughout seed development (Figures 5O and 5P). Thus, these results implicate DOF TFs as key upstream regulators of sugar transporters, including *GmSWEET10a* and *GmSWEET15a*, and a central role in coordinating nutrient transfer to the developing embryo.

Developmental trajectories defining soybean embryogenesis

Many important soybean agronomic traits are established during embryogenesis. However, the regulatory and gene expression dynamics underlying cellular diversification during embryogenesis remain unresolved. Motivated by this question, we isolated all embryo-related nuclei across the four stages (globular, heart, cotyledon, and early maturation) of seed development and performed an integration across scATAC-seq and snRNA-seq modalities (Figures S6L and S6M; Table S1). To improve the resolution of developmental progression, we inferred the precise developmental age of each nucleus using a recently described least absolute shrinkage and selection operator (LASSO) regression approach (Figure 6A).[70] The predicted continuous developmental ages from the full dataset (Pearson's correlation = 0.93) and withheld test nuclei (Pearson's correlation = 0.96) were highly correlated with the known seed stage (Figures 6B and S6N). We identified 248 genes predictive of developmental age and uncovered the sequential gene expression dynamics associated with overall developmental progression regardless of cell lineage (Figures 6C and 6D), thereby providing a useful benchmark for anchoring analyses of cellular diversification during embryogenesis.

Evaluation of cellular diversity across the four seed stages of embryogenesis revealed five distinct developmental branches (Figure 6E). To determine the regulatory and gene expression dynamics that make these lineages distinct from others, we constructed pseudotime trajectories for each individual branch using the snRNA-seq nuclei as a reference. Indicating a firm biological foundation, we observed a strong positive trend between pseudotime scores and inferred developmental age (Figures 6F and 6G). Interestingly, we found a strong negative correlation between transcriptional complexity and inferred developmental age, a notable feature of cell differentiation in mammals[70] that appears to be conserved in plants (Figure S6O). Hypothesizing that cellular diversification would be accompanied by the acquisition of specialized gene expression programs, we identified differentially expressed genes across pseudotime for each individual branch. Indeed, visualization of pseudotime-associated genes revealed distinct transcription signatures hallmarking each lineage (Figure 6H). Importantly, we found that several well-known marker genes displayed expected developmental transcription patterns, including *LATE EMBRYOGENESIS ABUNDANT 26* (*LEA26*) in cotyledon parenchyma,[71] *PROTODERMAL FACTOR 1* (*PDF1*) in the protoderm, *MONOPTEROS* (*MP*) in provascular, and *PLETHORA2* (*PLT2*) in shoot/RAM trajectories that collectively support robust trajectory ordering (Figure 6I).[72]

Specification of the developing cotyledon parenchyma has been posited as a key developmental event that determines nutrient composition of mature seeds (Figure 6E).[73] We hypothesized that detailed interrogation of the regulatory dynamics

(N) Correlation heatmap between TF motif deviation scores and pseudotime-associated genes aligned by pseudotime for peripheral endosperm. PCC, Pearson's correlation coefficient.
(O) Expression of *GmDOF11 (08G276300)*, DOF-MA1278 motif deviation, and expression of its putative target genes *GmSWEET10a* and *GmSWEET15a*. The DOF-MA1278 motif is shown above.
(P) Pseudobulk cell-type Tn5 integration site coverage around *GmSWEET10a* and *GmSWEET15a* across the four seed stages.
See also Figure S6 and Table S5.

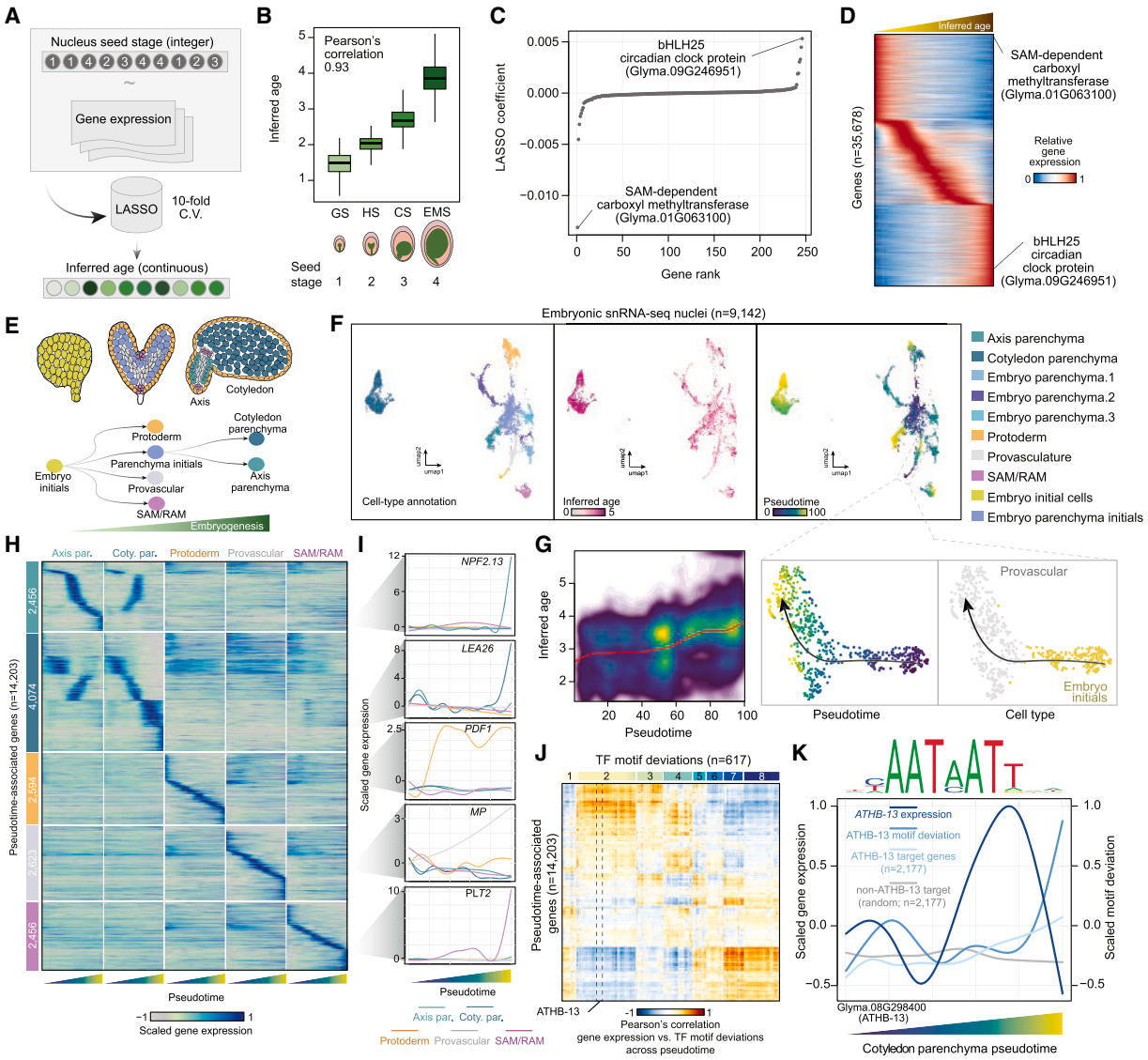

Figure 6. Developmental trajectories defining soybean embryogenesis

(A) Illustration of LASSO models to learn continuous representations of nuclei age.
(B) Comparison of inferred nuclei age and categorical seed stages.
(C) LASSO coefficient ranks of genes toward inferred nuclei ages.
(D) Heatmap of relative gene expression levels ordered by nuclei age.
(E) Schematic of embryogenesis trajectories.
(F) UMAP scatterplots of cell-type annotation (left), inferred nuclei age (middle), and pseudotime (right) for embryonic snRNA-seq nuclei.
(G) Comparison of inferred age and pseudotime scores across all embryonic nuclei.
(H) Heatmap of pseudotime-associated genes (FDR < 0.05) for all five trajectories.
(I) Exemplary gene expression profiles across pseudotime for five marker genes.
(J) Correlation heatmap between TF motif deviation scores and pseudotime-associated genes aligned by cotyledon parenchyma pseudotime.
(K) *ATHB-13* gene expression, ATHB-13 motif deviation, ATHB-13 target gene expression, and control gene expression profiles across cotyledon parenchyma developmental pseudotime. The motif recognized by ATHB-13 is shown above.
See also Figure S6 and Table S1.

between cotyledon and axis parenchyma would be informative for understanding the divergence of these tissues during embryogenesis and uncover ideal targets for soybean improvement efforts. To this end, we imputed TF motif deviations from scATAC-seq onto co-embedded snRNA-seq nuclei (Figures S6P and S6S) and identified TF motif deviations and gene expression patterns that were correlated across pseudotime for the cotyledon parenchyma trajectory (Figure 6J). This analysis revealed eight TF modules associated with largely distinct gene sets, representing putative gene regulatory networks

underlying cotyledon parenchyma development. Next, we speculated that temporal gene expression divergence between axis and cotyledon parenchyma could identify genes associated with lineage bifurcation of parenchyma initials. By comparing temporal gene expression between axis and cotyledon parenchyma, using each branch as a reference (Figure S6R), we found similar gene expression patterns between axis and cotyledon parenchyma early in both trajectories. However, we identified a decrease in temporal gene expression correlations approximately 60% of the way through both trajectories aligning with visual differences in branch-specific genes and the onset of parenchyma initials bifurcation (Figures S6Q and S6R). Further dissection of this pseudotime point revealed that a homolog of *ATHB-13* (hereafter referred to as *GmATHB13*) was the first TF to be differentially expressed between axis and cotyledon parenchyma at parenchyma initials bifurcation. Interestingly, *ATHB-13* is an HD-Zip I TF previously associated with cotyledon morphogenesis in *Arabidopsis*,[74] and null alleles of *ATHB-13* exhibit increased root length[75] which develops from the axis tissue in soybean seed. Thus, we hypothesized that *GmATHB13* acts as a negative regulator of axis development by promoting cotyledon parenchyma identity.

Next, to showcase the power of pseudotime analysis for understanding cellular differentiation, we aimed to characterize the targets and dynamics of GmATHB13 across cotyledon parenchyma development. First, we defined the putative targets of GmATHB13 as the set of expressed genes within the cotyledon parenchyma trajectory with nearby ACRs containing the ATHB13 motif (n = 2,177), as well as a set of cotyledon parenchyma expressed control 'non-target' genes (n = 2,177) lacking ATHB13 motifs within nearby ACRs (Figure 6K). Consistent with the known function of cotyledon parenchyma, expressed genes with accessible ATHB13 motifs were enriched for GO terms related to carbohydrate, polysaccharide, glycogen, and energy reserve metabolic processes. We then evaluated expression and TF motif deviation dynamics of ATHB13 in unison with the expression patterns of putative ATHB13 targets and the set of control genes (Figure 6K). *GmATHB13* is initially expressed at low levels and then reaches a peak immediately after the bifurcation point that is followed by a rapid decrease, indicating that *GmATHB13* expression is tightly correlated with bifurcation of parenchyma initials in a dose-dependent manner. Global chromatin accessibility of the ATHB13 motif increased following the peak of *GmATHB13* expression, suggesting a genome-wide increase in ATHB13 DNA-binding activity that depends on *GmATHB13* transcript levels. Finally, putative ATHB13 targets show higher levels of expression compared with the control set following bifurcation, implicating GmATHB13 as a transcriptional activator. Collectively, these data suggest that the expression of *GmATHB13* in parenchyma initials above a dosage threshold results in the activation of a gene expression program that promotes cotyledon parenchyma identity.

DISCUSSION

In-depth knowledge of cell-type resolved transcriptional regulatory programs is essential for gene function studies and gene regulatory network discovery, which are key to both developmental biology and crop improvement.[76] Here, we constructed a comprehensive single-cell CRE and gene expression atlas by integrating single-cell genomic and spatial technology, profiling 316,358 cells across ten primary tissues in soybean. We assessed the accessibility of approximately 300,000 ACRs across 103 cell types, measuring the cell-type-specific CRE activity that drives dynamic gene expression from the soybean genome. This ACR atlas represents a valuable resource for the soybean community to understand the molecular patterns underlying cell-type diversification in soybean. Additionally, this work provides a framework for constructing cell-type-specific *cis*-regulatory maps for other non-model species lacking known functional marker genes.

The cell-type-resolved ACR atlas offers a comprehensive roadmap for studying gene regulatory dynamics across cell types and developmental stages, with important implications for gene expression manipulation during crop improvement, potential cell-type regulator discovery, and synthetic biology applications. For example, genome editing of CREs allows for the altered regulation of target genes, leading to phenotypic variations that are valuable for improving traits related to yield and plant architecture.[77–79] Using data from infected cells in developing nodules, we identified four TF motifs of known master regulators of nodulation and discovered two unknown TF motifs specific to infected cells, which likely play roles in symbiotic nitrogen fixation. Furthermore, this atlas provides a rich resource for identifying cell-type-specific enhancers, which are of significant interest in both gene regulation and synthetic biology.[80] Most ctACRs were associated with distal genes, suggesting that distal chromatin-chromatin interactions may play a role in mediating spatiotemporal gene expression. This highlights the potential need of further developing single-cell chromatin interaction profiling methods in plants.

Integrating single-cell gene expression with chromatin accessibility data can greatly enhance gene regulatory network inference at an unprecedented resolution.[81] Our multi-omic atlas demonstrates several approaches for inferring gene regulatory networks: A. Recapitulating known networks: we *de novo* identified four TF motifs of known master regulators of nodulation and located their binding sites in the ACRs of their target genes, reflecting similar regulatory patterns found in *Medicago truncatula* and *Lotus japonicus* after decades of research. B. Identifying upstream regulators: we identified 13 sucrose transporters with shared expression patterns and a common TF binding site for DOF TFs in their candidate CREs. This aligns with previous findings where OsDof11 regulates sugar transporter genes and rice seed size,[82] suggesting that the DOF-SWEET regulatory axis may be conserved across monocots and dicots. C. Discovering cell-type regulators: through pseudotime trajectory analysis, we identified GmATHB-13 as a potential regulator of the bifurcation between axis and cotyledon parenchyma lineages, aligning with its known role in promoting cotyledon morphogenesis and negatively regulating root development in *Arabidopsis*. Genes containing accessible ATHB-13 motifs were enriched in carbohydrate and polysaccharide metabolism, which supports the energy production and storage functions of soybean cotyledon parenchyma cells. Our analyses are just a starting point, with many other insights to be discovered from these data by exploring the expression patterns and regulatory networks of other genes of interest.

To facilitate future discovery, we constructed a soybean multi-omic atlas database (https://soybean-atlas.com/), which includes chromatin accessibility and gene expression data for all the cell types explored here. For example, by leveraging the database, we predicted the gene regulatory network for LEAFY COTYLEDON1 (LEC1), a key regulator of embryo and endosperm development[83] (Figure S7). We identified two ACRs in the first intron of the *LEC1* paralogs, specifically accessible in endosperm and embryo cells, along with motifs for GmABI3a and GmMYB118, which regulate embryo[28,84] and endosperm development,[49] respectively. Thus, we can propose a model that the intronic ABI3 and MYB118 motifs contribute to the spatial and temporal regulation of *LEC1* expression during seed development (Figure S7). The interactive website makes it easy for researchers to explore gene regulatory networks at cell-type resolution for various soybean traits.

Additionally, all preprocessed data matrices, including ctACRs, genes, and TF motifs, are also accessible through The National Center for Biotechnology Information[85] (NCBI GEO: GSE270392) and SoyBase (https://www.soybase.org/).[86] We anticipate that the real potential of single-cell methods will extend beyond aiding gene function studies and uncovering regulatory networks. It will involve combining single-cell gene regulatory atlases with machine learning and high-throughput perturbation techniques to achieve a profound and predictive understanding of gene regulation throughout plant development that can be used to precisely improve crop performance.

Limitations of the study

Although we profiled single-cell transcriptome and chromatin accessibility from tissues at the same developmental stage, these two modalities were assessed separately, meaning they were not derived from the same individual cells. Instead, we relied on computational methods to integrate the datasets, which introduces potential limitations due to the inherent complexity and variability of these techniques. Additionally, we used spatial transcriptomics to validate cell-type identities in the single-cell datasets. However, the spatial transcriptomics data have a resolution of approximately 50 μm, which is generally larger than single-cell resolution. As a result, the validation is not at the level of individual cells, necessitating the use of prior marker information from other species to aid in the annotation. Although we assume that marker genes are expressed similarly across species, there is a risk of inaccuracies due to functional diversification over evolutionary time. These limitations, particularly the reliance on cross-species markers and the integration of separate modalities, could impact the precision of our findings. Additionally, inaccuracies in gene and TE annotations may have impacted our study by misidentifying or omitting key sequence elements, leading to potential misinterpretations of the data. However, we anticipate that future advancements in technology will help overcome these challenges, improving the accuracy and resolution of such studies.

RESOURCE AVAILABILITY

Lead contact

Further requests and information concerning this study should be addressed to the lead contact, Robert J. Schmitz (schmitz@uga.edu).

Materials availability

All the reagents are available on request to the lead contact, Robert J. Schmitz (schmitz@uga.edu).

Data and code availability

- All datasets generated in this study are available at GEO: GSE270392. All original code is deposited at GitHub (https://github.com/schmitzlab/soybean_atlas, https://doi.org/10.5281/zenodo.12571868). We created an interactive web soybean multi-omic atlas (https://soybean-atlas.com/).
- The genotype data for soybean haplotype map were downloaded from Figshare (https://figshare.com/projects/Soybean_Haplotype_Map_GmHapMap_A_Universal_Resource_for_Soybean_Translational_and_Functional_Genomics/56921).
- The laser-capture microdissection RNA-seq datasets were downloaded from GEO: GSE57349, GSE57350, GSE57606, GSE46906.

ACKNOWLEDGMENTS

We would like to acknowledge Dr. Jianxin Ma for sharing the *Bradyrhizobium japonicum* strain USDA110, Dr. Hang Yin for providing access to their cryostat, and Dr. Aaron Mitchell for access to their microscope. We especially express our appreciation to Dr. Robert B. Goldberg, Dr. John J. Harada, and Dr. Matteo Pellegrini for their pioneering work in "GENE NETWORKS IN SEED DEVELOPMENT" (http://seedgenenetwork.net/), which was critical for evaluating the quality of the single-cell genomic data and analysis. This research was supported by the United Soybean Board (2432-201-0102) and the National Science Foundation (IOS-1856627) to R.J.S. and the National Institute for General Medical Sciences of the National Institutes of Health (R00GM144742) to A.P.M.

AUTHOR CONTRIBUTIONS

R.J.S. and X.Z. designed the research. X.Z. and Z.L. performed the experiments. X.Z., Z.L., A.P.M., H.Y., H.J., S.B., J.P.M., M.A.A.M., and R.J.S. analyzed the data. X.Z., Z.L., A.P.M., and R.J.S. wrote the manuscript. The authors read and approved the final manuscript.

DECLARATION OF INTERESTS

R.J.S. is a co-founder of REquest Genomics, LLC, & Company, which provides epigenomic services.

STAR★METHODS

Detailed methods are provided in the online version of this paper and include the following:

- KEY RESOURCES TABLE
- EXPERIMENTAL MODEL AND STUDY PARTICIPANT DETAILS
  - Growth conditions
  - Soybean leaves
  - Soybean hypocotyls
  - Soybean roots
  - Soybean nodules
  - Soybean pods
  - Soybean seeds
- METHOD DETAILS
  - scATAC-seq library preparation
  - Bulk ATAC-seq library preparation
  - snRNA-seq library preparation
  - Spatial RNA-seq library preparation
  - Library preparation of whole genome bisulfite sequencing
- QUANTIFICATION AND STATISTICAL ANALYSIS
  - scATAC-seq raw reads processing
  - snRNA-seq raw reads processing
  - spRNA-seq reads processing

- DNA methylation analysis
- Integration of snRNA-seq and spRNA-seq
- *De novo* marker identification
- Cell-type annotation for snRNA-seq
- Cell-type annotation for scATAC-seq
- ACR identification
- Predicting the functions of ACRs
- Identification of whole genome duplication ACRs
- Identification of intergenic negative control regions
- Identification of cell-type-specific ACRs
- TF Motif deviations score calculation
- Motif enrichment
- *De novo* TF motif enrichment
- Embryo scATAC-seq and scRNA-seq clustering
- Embryo scATAC-seq and snRNA-seq integration
- Inferred developmental age of embryo nuclei
- Trajectory analysis

SUPPLEMENTAL INFORMATION

Supplemental information can be found online at https://doi.org/10.1016/j.cell.2024.10.050.

Received: July 2, 2024
Revised: September 26, 2024
Accepted: October 31, 2024
Published: December 31, 2024

REFERENCES

1. Schmitz, R.J., Grotewold, E., and Stam, M. (2022). Cis-regulatory sequences in plants: Their importance, discovery, and future challenges. Plant Cell *34*, 718–741. https://doi.org/10.1093/plcell/koab281.
2. Marand, A.P., Eveland, A.L., Kaufmann, K., and Springer, N.M. (2023). cis-Regulatory Elements in Plant Development, Adaptation, and Evolution. Annu. Rev. Plant Biol. *74*, 111–137. https://doi.org/10.1146/annurev-arplant-070122-030236.
3. Klemm, S.L., Shipony, Z., and Greenleaf, W.J. (2019). Chromatin accessibility and the regulatory epigenome. Nat. Rev. Genet. *20*, 207–220. https://doi.org/10.1038/s41576-018-0089-8.
4. Vandereyken, K., Sifrim, A., Thienpont, B., and Voet, T. (2023). Methods and applications for single-cell and spatial multi-omics. Nat. Rev. Genet. *24*, 494–515. https://doi.org/10.1038/s41576-023-00580-2.
5. Zhang, X., Marand, A.P., Yan, H., and Schmitz, R.J. (2024). scifi-ATAC-seq: massive-scale single-cell chromatin accessibility sequencing using combinatorial fluidic indexing. Genome Biol. *25*, 90. https://doi.org/10.1186/s13059-024-03235-5.
6. Hie, B., Peters, J., Nyquist, S.K., Shalek, A.K., Berger, B., and Bryson, B.D. (2020). Computational methods for single-cell RNA sequencing. Annu. Rev. Biomed. Data Sci. *3*, 339–364. https://doi.org/10.1146/annurev-biodatasci-012220-100601.
7. Cao, J., O'Day, D.R., Pliner, H.A., Kingsley, P.D., Deng, M., Daza, R.M., Zager, M.A., Aldinger, K.A., Blecher-Gonen, R., Zhang, F., et al. (2020). A human cell atlas of fetal gene expression. Science *370*, eaba7721. https://doi.org/10.1126/science.aba7721.
8. Zhang, K., Hocker, J.D., Miller, M., Hou, X., Chiou, J., Poirion, O.B., Qiu, Y., Li, Y.E., Gaulton, K.J., Wang, A., et al. (2021). A single-cell atlas of chromatin accessibility in the human genome. Cell *184*, 5985–6001.e19. https://doi.org/10.1016/j.cell.2021.10.024.
9. Yao, Z., Liu, H., Xie, F., Fischer, S., Adkins, R.S., Aldridge, A.I., Ament, S.A., Bartlett, A., Behrens, M.M., Van den Berge, K., et al. (2021). A transcriptomic and epigenomic cell atlas of the mouse primary motor cortex. Nature *598*, 103–110. https://doi.org/10.1038/s41586-021-03500-8.
10. Li, Y.E., Preissl, S., Miller, M., Johnson, N.D., Wang, Z., Jiao, H., Zhu, C., Wang, Z., Xie, Y., Poirion, O., et al. (2023). A comparative atlas of single-cell chromatin accessibility in the human brain. Science *382*, eadf7044. https://doi.org/10.1126/science.adf7044.
11. Cuperus, J.T. (2022). Single-cell genomics in plants: current state, future directions, and hurdles to overcome. Plant Physiol. *188*, 749–755. https://doi.org/10.1093/plphys/kiab478.
12. Shaw, R., Tian, X., and Xu, J. (2021). Single-Cell Transcriptome Analysis in Plants: Advances and Challenges. Mol. Plant *14*, 115–126. https://doi.org/10.1016/j.molp.2020.10.012.
13. Bang, S., Zhang, X., Gregory, J., Chen, Z., Galli, M., Gallavotti, A., and Schmitz, R.J. (2024). WUSCHEL dependent chromatin regulation in maize inflorescence development at single-cell resolution. Preprint at bioRxiv. https://doi.org/10.1101/2024.05.13.593957.
14. Mendieta, J.P., Tu, X., Jiang, D., Yan, H., Zhang, X., Marand, A.P., Zhong, S., and Schmitz, R.J. (2024). Investigating the cis-Regulatory Basis of C3 and C4 Photosynthesis in Grasses at Single-Cell Resolution. Preprint at bioRxiv. https://doi.org/10.1101/2024.01.05.574340.
15. Farmer, A., Thibivilliers, S., Ryu, K.H., Schiefelbein, J., and Libault, M. (2021). Single-nucleus RNA and ATAC sequencing reveals the impact of chromatin accessibility on gene expression in Arabidopsis roots at the single-cell level. Mol. Plant *14*, 372–383. https://doi.org/10.1016/j.molp.2021.01.001.
16. Shahan, R., Hsu, C.W., Nolan, T.M., Cole, B.J., Taylor, I.W., Greenstreet, L., Zhang, S., Afanassiev, A., Vlot, A.H.C., Schiebinger, G., et al. (2022). A single-cell Arabidopsis root atlas reveals developmental trajectories in wild-type and cell identity mutants. Dev. Cell *57*, 543–560.e9. https://doi.org/10.1016/j.devcel.2022.01.008.
17. Xu, X., Crow, M., Rice, B.R., Li, F., Harris, B., Liu, L., Demesa-Arevalo, E., Lu, Z., Wang, L., Fox, N., et al. (2021). Single-cell RNA sequencing of developing maize ears facilitates functional analysis and trait candidate gene discovery. Dev. Cell *56*, 557–568.e6. https://doi.org/10.1016/j.devcel.2020.12.015.
18. Lee, T.A., Nobori, T., Illouz-Eliaz, N., Xu, J., Jow, B., Nery, J.R., and Ecker, J.R. (2023). A single-nucleus atlas of seed-to-seed development in Arabidopsis. Preprint at bioRxiv.
19. Marand, A.P., Chen, Z., Gallavotti, A., and Schmitz, R.J. (2021). A cis-regulatory atlas in maize at single-cell resolution. Cell *184*, 3041–3055.e21. https://doi.org/10.1016/j.cell.2021.04.014.
20. Yan, H., Mendieta, J.P., Zhang, X., Marand, A.P., Liang, Y., Luo, Z., Minow, M.A.A., Jang, H., Li, X., Roule, T., et al. (2024). Evolution of plant cell-type-specific cis -regulatory elements. Preprint at bioRxiv. https://doi.org/10.1101/2024.01.08.574753.
21. Mendieta, J.P., Sangra, A., Yan, H., Minow, M.A.A., and Schmitz, R.J. (2023). Exploring plant cis-regulatory elements at single-cell resolution: overcoming biological and computational challenges to advance plant research. Plant J. *115*, 1486–1499. https://doi.org/10.1111/tpj.16351.
22. Liu, Z., Kong, X., Long, Y., Liu, S., Zhang, H., Jia, J., Cui, W., Zhang, Z., Song, X., Qiu, L., et al. (2023). Integrated single-nucleus and spatial transcriptomics captures transitional states in soybean nodule maturation. Nat. Plants *9*, 515–524. https://doi.org/10.1038/s41477-023-01387-z.
23. Yu, X., Liu, Z., and Sun, X. (2023). Single-cell and spatial multi-omics in the plant sciences: Technical advances, applications, and perspectives. Plant Commun. *4*, 100508. https://doi.org/10.1016/j.xplc.2022.100508.
24. Wang, Y., Luo, Y., Guo, X., Li, Y., Yan, J., Shao, W., Wei, W., Wei, X., Yang, T., Chen, J., et al. (2024). A spatial transcriptome map of the developing maize ear. Nat. Plants *10*, 815–827. https://doi.org/10.1038/s41477-024-01683-2.
25. Schmutz, J., Cannon, S.B., Schlueter, J., Ma, J., Mitros, T., Nelson, W., Hyten, D.L., Song, Q., Thelen, J.J., Cheng, J., et al. (2010). Genome sequence of the palaeopolyploid soybean. Nature *463*, 178–183. https://doi.org/10.1038/nature08670.
26. Hao, Y., Hao, S., Andersen-Nissen, E., Mauck, W.M., 3rd, Zheng, S., Butler, A., Lee, M.J., Wilk, A.J., Darby, C., Zager, M., et al. (2021). Integrated

analysis of multimodal single-cell data. Cell *184*, 3573–3587.e29. https://doi.org/10.1016/j.cell.2021.04.048.

27. Danzer, J., Mellott, E., Bui, A.Q., Le, B.H., Martin, P., Hashimoto, M., Perez-Lesher, J., Chen, M., Pelletier, J.M., Somers, D.A., et al. (2015). Down-Regulating the Expression of 53 Soybean Transcription Factor Genes Uncovers a Role for SPEECHLESS in Initiating Stomatal Cell Lineages during Embryo Development. Plant Physiol. *168*, 1025–1035. https://doi.org/10.1104/pp.15.00432.
28. Jo, L., Pelletier, J.M., Hsu, S.W., Baden, R., Goldberg, R.B., and Harada, J.J. (2020). Combinatorial interactions of the LEC1 transcription factor specify diverse developmental programs during soybean seed development. Proc. Natl. Acad. Sci. USA *117*, 1223–1232. https://doi.org/10.1073/pnas.1918441117.
29. Wang, S., Yokosho, K., Guo, R., Whelan, J., Ruan, Y.L., Ma, J.F., and Shou, H. (2019). The Soybean Sugar Transporter GmSWEET15 Mediates Sucrose Export from Endosperm to Early Embryo. Plant Physiol. *180*, 2133–2141. https://doi.org/10.1104/pp.19.00641.
30. Li, J., Wang, Q., An, Y., Chen, X., Xing, Y., Deng, Q., Li, Z., Wang, S., Dai, X., Liang, N., et al. (2022). Integrative Single-Cell RNA-Seq and ATAC-Seq Analysis of Mesenchymal Stem/Stromal Cells Derived from Human Placenta. Front. Cell Dev. Biol. *10*, 836887. https://doi.org/10.3389/fcell.2022.836887.
31. Perez-Grau, L., and Goldberg, R.B. (1989). Soybean Seed Protein Genes Are Regulated Spatially during Embryogenesis. Plant Cell *1*, 1095–1109. https://doi.org/10.1105/tpc.1.11.1095.
32. Aida, M., Beis, D., Heidstra, R., Willemsen, V., Blilou, I., Galinha, C., Nussaume, L., Noh, Y.S., Amasino, R., and Scheres, B. (2004). The PLETHORA genes mediate patterning of the Arabidopsis root stem cell niche. Cell *119*, 109–120. https://doi.org/10.1016/j.cell.2004.09.018.
33. Wang, S., Liu, S., Wang, J., Yokosho, K., Zhou, B., Yu, Y.C., Liu, Z., Frommer, W.B., Ma, J.F., Chen, L.Q., et al. (2020). Simultaneous changes in seed size, oil content and protein content driven by selection of SWEET homologues during soybean domestication. Natl. Sci. Rev. *7*, 1776–1786. https://doi.org/10.1093/nsr/nwaa110.
34. Torkamaneh, D., Laroche, J., Valliyodan, B., O'Donoughue, L., Cober, E., Rajcan, I., Vilela Abdelnoor, R., Sreedasyam, A., Schmutz, J., Nguyen, H.T., and Belzile, F. (2021). Soybean (Glycine max) Haplotype Map (GmHapMap): a universal resource for soybean translational and functional genomics. Plant Biotechnol. J. *19*, 324–334. https://doi.org/10.1111/pbi.13466.
35. Marand, A.P., and Schmitz, R.J. (2022). Single-cell analysis of cis-regulatory elements. Curr. Opin. Plant Biol. *65*, 102094. https://doi.org/10.1016/j.pbi.2021.102094.
36. Fang, C., Yang, M., Tang, Y., Zhang, L., Zhao, H., Ni, H., Chen, Q., Meng, F., and Jiang, J. (2023). Dynamics of cis-regulatory sequences and transcriptional divergence of duplicated genes in soybean. Proc. Natl. Acad. Sci. USA *120*, e2303836120. https://doi.org/10.1073/pnas.2303836120.
37. Soyano, T., Shimoda, Y., Kawaguchi, M., and Hayashi, M. (2019). A shared gene drives lateral root development and root nodule symbiosis pathways in Lotus. Science *366*, 1021–1023. https://doi.org/10.1126/science.aax2153.
38. Dong, Y., Yang, X., Liu, J., Wang, B.H., Liu, B.L., and Wang, Y.Z. (2014). Pod shattering resistance associated with domestication is mediated by a NAC gene in soybean. Nat. Commun. *5*, 3352. https://doi.org/10.1038/ncomms4352.
39. Rauf, M., Arif, M., Fisahn, J., Xue, G.P., Balazadeh, S., and Mueller-Roeber, B. (2013). NAC transcription factor speedy hyponastic growth regulates flooding-induced leaf movement in Arabidopsis. Plant Cell *25*, 4941–4955. https://doi.org/10.1105/tpc.113.117861.
40. Liu, Y., Peng, X., Ma, A., Liu, W., Liu, B., Yun, D.J., and Xu, Z.Y. (2023). Type-B response regulator OsRR22 forms a transcriptional activation complex with OsSLR1 to modulate OsHKT2;1 expression in rice. Sci. China Life Sci. *66*, 2922–2934. https://doi.org/10.1007/s11427-023-2464-2.
41. Mara, C.D., Huang, T., and Irish, V.F. (2010). The Arabidopsis floral homeotic proteins APETALA3 and PISTILLATA negatively regulate the BANQUO genes implicated in light signaling. Plant Cell *22*, 690–702. https://doi.org/10.1105/tpc.109.065946.
42. Zhao, P.X., Zhang, J., Chen, S.Y., Wu, J., Xia, J.Q., Sun, L.Q., Ma, S.S., and Xiang, C.B. (2021). Arabidopsis MADS-box factor AGL16 is a negative regulator of plant response to salt stress by downregulating salt-responsive genes. New Phytol. *232*, 2418–2439. https://doi.org/10.1111/nph.17760.
43. Ng, M., and Yanofsky, M.F. (2001). Function and evolution of the plant MADS-box gene family. Nat. Rev. Genet. *2*, 186–195. https://doi.org/10.1038/35056041.
44. Lu, Z., Marand, A.P., Ricci, W.A., Ethridge, C.L., Zhang, X., and Schmitz, R.J. (2019). The prevalence, evolution and chromatin signatures of plant regulatory elements. Nat. Plants *5*, 1250–1259. https://doi.org/10.1038/s41477-019-0548-z.
45. Fueyo, R., Judd, J., Feschotte, C., and Wysocka, J. (2022). Roles of transposable elements in the regulation of mammalian transcription. Nat. Rev. Mol. Cell Biol. *23*, 481–497. https://doi.org/10.1038/s41580-022-00457-y.
46. Ricci, W.A., Lu, Z., Ji, L., Marand, A.P., Ethridge, C.L., Murphy, N.G., Noshay, J.M., Galli, M., Mejía-Guerra, M.K., Colomé-Tatché, M., et al. (2019). Widespread long-range cis-regulatory elements in the maize genome. Nat. Plants *5*, 1237–1249. https://doi.org/10.1038/s41477-019-0547-0.
47. Rauluseviciute, I., Riudavets-Puig, R., Blanc-Mathieu, R., Castro-Mondragon, J.A., Ferenc, K., Kumar, V., Lemma, R.B., Lucas, J., Chèneby, J., Baranasic, D., et al. (2024). JASPAR 2024: 20th anniversary of the open-access database of transcription factor binding profiles. Nucleic Acids Res. *52*, D174–D182. https://doi.org/10.1093/nar/gkad1059.
48. Khosla, A., Paper, J.M., Boehler, A.P., Bradley, A.M., Neumann, T.R., and Schrick, K. (2014). HD-Zip Proteins GL2 and HDG11 Have Redundant Functions in Arabidopsis Trichomes, and GL2 Activates a Positive Feedback Loop via MYB23. Plant Cell *26*, 2184–2200. https://doi.org/10.1105/tpc.113.120360.
49. Barthole, G., To, A., Marchive, C., Brunaud, V., Soubigou-Taconnat, L., Berger, N., Dubreucq, B., Lepiniec, L., and Baud, S. (2014). MYB118 represses endosperm maturation in seeds of Arabidopsis. Plant Cell *26*, 3519–3537. https://doi.org/10.1105/tpc.114.130021.
50. Roy, S., Liu, W., Nandety, R.S., Crook, A., Mysore, K.S., Pislariu, C.I., Frugoli, J., Dickstein, R., and Udvardi, M.K. (2020). Celebrating 20 Years of Genetic Discoveries in Legume Nodulation and Symbiotic Nitrogen Fixation. Plant Cell *32*, 15–41. https://doi.org/10.1105/tpc.19.00279.
51. Wu, X., Xiong, Y., Lu, J., Yang, M., Ji, H., Li, X., and Wang, Z. (2023). GmNLP7a inhibits soybean nodulation by interacting with GmNIN1a. Crop J. *11*, 1401–1410. https://doi.org/10.1016/j.cj.2023.03.016.
52. Nishida, H., Nosaki, S., Suzuki, T., Ito, M., Miyakawa, T., Nomoto, M., Tada, Y., Miura, K., Tanokura, M., Kawaguchi, M., and Suzaki, T. (2021). Different DNA-binding specificities of NLP and NIN transcription factors underlie nitrate-induced control of root nodulation. Plant Cell *33*, 2340–2359. https://doi.org/10.1093/plcell/koab103.
53. Zhao, J., Favero, D.S., Peng, H., and Neff, M.M. (2013). Arabidopsis thaliana AHL family modulates hypocotyl growth redundantly by interacting with each other via the PPC/DUF296 domain. Proc. Natl. Acad. Sci. USA *110*, E4688–E4697. https://doi.org/10.1073/pnas.1219277110.
54. Kubo, H., Peeters, A.J., Aarts, M.G., Pereira, A., and Koornneef, M. (1999). ANTHOCYANINLESS2, a homeobox gene affecting anthocyanin distribution and root development in Arabidopsis. Plant Cell *11*, 1217–1226. https://doi.org/10.1105/tpc.11.7.1217.
55. Andriankaja, A., Boisson-Dernier, A., Frances, L., Sauviac, L., Jauneau, A., Barker, D.G., and de Carvalho-Niebel, F. (2007). AP2-ERF transcription factors mediate Nod factor dependent Mt ENOD11 activation in root hairs via a novel cis-regulatory motif. Plant Cell *19*, 2866–2885. https://doi.org/10.1105/tpc.107.052944.

56. Doll, N.M., and Ingram, G.C. (2022). Embryo–endosperm interactions. Annu. Rev. Plant Biol. *73*, 293–321. https://doi.org/10.1146/annurev-arplant-102820-091838.

57. Povilus, R.A., and Gehring, M. (2022). Maternal-filial transfer structures in endosperm: A nexus of nutritional dynamics and seed development. Curr. Opin. Plant Biol. *65*, 102121. https://doi.org/10.1016/j.pbi.2021.102121.

58. Picard, C.L., Povilus, R.A., Williams, B.P., and Gehring, M. (2021). Transcriptional and imprinting complexity in Arabidopsis seeds at single-nucleus resolution. Nat. Plants *7*, 730–738. https://doi.org/10.1038/s41477-021-00922-0.

59. Dute, R.R., and Peterson, C.M. (1992). Early Endosperm Development in Ovules of Soybean, Glycine max (L) Merr. (Fabaceae)*. Ann. Bot. *69*, 263–271. https://doi.org/10.1093/oxfordjournals.aob.a088339.

60. Belmonte, M.F., Kirkbride, R.C., Stone, S.L., Pelletier, J.M., Bui, A.Q., Yeung, E.C., Hashimoto, M., Fei, J., Harada, C.M., Munoz, M.D., et al. (2013). Comprehensive developmental profiles of gene activity in regions and subregions of the Arabidopsis seed. Proc. Natl. Acad. Sci. USA *110*, E435–E444. https://doi.org/10.1073/pnas.1222061110.

61. Nguyen, H., Brown, R.C., and Lemmon, B.E. (2000). The specialized chalazal endosperm in Arabidopsis thaliana and Lepidium virginicum (Brassicaceae). Protoplasma *212*, 99–110. https://doi.org/10.1007/BF01279351.

62. Doll, N.M., Royek, S., Fujita, S., Okuda, S., Chamot, S., Stintzi, A., Widiez, T., Hothorn, M., Schaller, A., Geldner, N., and Ingram, G. (2020). A two-way molecular dialogue between embryo and endosperm is required for seed development. Science *367*, 431–435. https://doi.org/10.1126/science.aaz4131.

63. Doll, N.M., and Nowack, M.K. (2024). Endosperm cell death: roles and regulation in angiosperms. J. Exp. Bot. *75*, 4346–4359. https://doi.org/10.1093/jxb/erae052.

64. Xiong, H., Wang, W., and Sun, M.X. (2021). Endosperm development is an autonomously programmed process independent of embryogenesis. Plant Cell *33*, 1151–1160. https://doi.org/10.1093/plcell/koab007.

65. Buono, R.A., Hudecek, R., and Nowack, M.K. (2019). Plant proteases during developmental programmed cell death. J. Exp. Bot. *70*, 2097–2112. https://doi.org/10.1093/jxb/erz072.

66. Patil, G., Valliyodan, B., Deshmukh, R., Prince, S., Nicander, B., Zhao, M., Sonah, H., Song, L., Lin, L., Chaudhary, J., et al. (2015). Soybean (Glycine max) SWEET gene family: insights through comparative genomics, transcriptome profiling and whole genome re-sequence analysis. BMC Genomics *16*, 520. https://doi.org/10.1186/s12864-015-1730-y.

67. Braun, D.M. (2022). Phloem Loading and Unloading of Sucrose: What a Long, Strange Trip from Source to Sink. Annu. Rev. Plant Biol. *73*, 553–584. https://doi.org/10.1146/annurev-arplant-070721-083240.

68. Julius, B.T., Leach, K.A., Tran, T.M., Mertz, R.A., and Braun, D.M. (2017). Sugar Transporters in Plants: New Insights and Discoveries. Plant Cell Physiol. *58*, 1442–1460. https://doi.org/10.1093/pcp/pcx090.

69. Wang, H.W., Zhang, B., Hao, Y.J., Huang, J., Tian, A.G., Liao, Y., Zhang, J.S., and Chen, S.Y. (2007). The soybean Dof-type transcription factor genes, GmDof4 and GmDof11, enhance lipid content in the seeds of transgenic Arabidopsis plants. Plant J. *52*, 716–729. https://doi.org/10.1111/j.1365-313X.2007.03268.x.

70. Calderon, D., Blecher-Gonen, R., Huang, X., Secchia, S., Kentro, J., Daza, R.M., Martin, B., Dulja, A., Schaub, C., Trapnell, C., et al. (2022). The continuum of Drosophila embryonic development at single-cell resolution. Science *377*, eabn5800. https://doi.org/10.1126/science.abn5800.

71. Candat, A., Paszkiewicz, G., Neveu, M., Gautier, R., Logan, D.C., Avelange-Macherel, M.H., and Macherel, D. (2014). The ubiquitous distribution of late embryogenesis abundant proteins across cell compartments in Arabidopsis offers tailored protection against abiotic stress. Plant Cell *26*, 3148–3166. https://doi.org/10.1105/tpc.114.127316.

72. ten Hove, C.A., Lu, K.J., and Weijers, D. (2015). Building a plant: cell fate specification in the early Arabidopsis embryo. Development *142*, 420–430. https://doi.org/10.1242/dev.111500.

73. Nguyen, Q.T., Kisiala, A., Andreas, P., Neil Emery, R.J., and Narine, S. (2016). Soybean seed development: fatty acid and phytohormone metabolism and their interactions. Curr. Genomics *17*, 241–260. https://doi.org/10.2174/1389202917666160202220238.

74. Le, B.H., Cheng, C., Bui, A.Q., Wagmaister, J.A., Henry, K.F., Pelletier, J., Kwong, L., Belmonte, M., Kirkbride, R., Horvath, S., et al. (2010). Global analysis of gene activity during Arabidopsis seed development and identification of seed-specific transcription factors. Proc. Natl. Acad. Sci. USA *107*, 8063–8070. https://doi.org/10.1073/pnas.1003530107.

75. Silva, A.T., Ribone, P.A., Chan, R.L., Ligterink, W., and Hilhorst, H.W.M. (2016). A Predictive Coexpression Network Identifies Novel Genes Controlling the Seed-to-Seedling Phase Transition in Arabidopsis thaliana. Plant Physiol. *170*, 2218–2231. https://doi.org/10.1104/pp.15.01704.

76. Purugganan, M.D., and Jackson, S.A. (2021). Advancing crop genomics from lab to field. Nat. Genet. *53*, 595–601. https://doi.org/10.1038/s41588-021-00866-3.

77. Chen, Y.H., Lu, J., Yang, X., Huang, L.C., Zhang, C.Q., Liu, Q.Q., and Li, Q.F. (2023). Gene editing of non-coding regulatory DNA and its application in crop improvement. J. Exp. Bot. *74*, 6158–6175. https://doi.org/10.1093/jxb/erad313.

78. Rodríguez-Leal, D., Lemmon, Z.H., Man, J., Bartlett, M.E., and Lippman, Z.B. (2017). Engineering Quantitative Trait Variation for Crop Improvement by Genome Editing. Cell *171*, 470–480.e8. https://doi.org/10.1016/j.cell.2017.08.030.

79. Liu, L., Gallagher, J., Arevalo, E.D., Chen, R., Skopelitis, T., Wu, Q., Bartlett, M., and Jackson, D. (2021). Enhancing grain-yield-related traits by CRISPR-Cas9 promoter editing of maize CLE genes. Nat. Plants *7*, 287–294. https://doi.org/10.1038/s41477-021-00858-5.

80. Despang, A. (2024). Designer enhancers for cell-type-specific gene regulation. Nat. Biotechnol. *42*, 31. https://doi.org/10.1038/s41587-023-02112-z.

81. Badia-I-Mompel, P., Wessels, L., Müller-Dott, S., Trimbour, R., Ramirez Flores, R.O., Argelaguet, R., and Saez-Rodriguez, J. (2023). Gene regulatory network inference in the era of single-cell multi-omics. Nat. Rev. Genet. *24*, 739–754. https://doi.org/10.1038/s41576-023-00618-5.

82. Wu, Y., Lee, S.K., Yoo, Y., Wei, J., Kwon, S.Y., Lee, S.W., Jeon, J.S., and An, G. (2018). Rice Transcription Factor OsDOF11 Modulates Sugar Transport by Promoting Expression of Sucrose Transporter and SWEET Genes. Mol. Plant *11*, 833–845. https://doi.org/10.1016/j.molp.2018.04.002.

83. Jo, L., Pelletier, J.M., and Harada, J.J. (2019). Central role of the LEAFY COTYLEDON1 transcription factor in seed development. J. Integr. Plant Biol. *61*, 564–580. https://doi.org/10.1111/jipb.12806.

84. Zhang, D., Zhao, M., Li, S., Sun, L., Wang, W., Cai, C., Dierking, E.C., and Ma, J. (2017). Plasticity and innovation of regulatory mechanisms underlying seed oil content mediated by duplicated genes in the palaeopolyploid soybean. Plant J. *90*, 1120–1133. https://doi.org/10.1111/tpj.13533.

85. Sayers, E.W., Beck, J., Bolton, E.E., Brister, J.R., Chan, J., Comeau, D.C., Connor, R., DiCuccio, M., Farrell, C.M., Feldgarden, M., et al. (2024). Database resources of the National Center for Biotechnology Information. Nucleic Acids Res. *52*, D33–D43. https://doi.org/10.1093/nar/gkad1044.

86. Brown, A.V., Conners, S.I., Huang, W., Wilkey, A.P., Grant, D., Weeks, N.T., Cannon, S.B., Graham, M.A., and Nelson, R.T. (2021). A new decade and new data at SoyBase, the USDA-ARS soybean genetics and genomics database. Nucleic Acids Res. *49*, D1496–D1501. https://doi.org/10.1093/nar/gkaa1107.

87. Blibaum, A., Werner, J., and Dobin, A. (2019). STARsolo: single-cell RNA-seq analyses beyond gene expression. Genome Inform. *5*, 10–11.

88. Danecek, P., Bonfield, J.K., Liddle, J., Marshall, J., Ohan, V., Pollard, M.O., Whitwham, A., Keane, T., McCarthy, S.A., Davies, R.M., et al. (2021). Twelve years of SAMtools and BCFtools. GigaScience *10*, giab008. https://doi.org/10.1093/gigascience/giab008.

89. Schultz, M.D., He, Y., Whitaker, J.W., Hariharan, M., Mukamel, E.A., Leung, D., Rajagopal, N., Nery, J.R., Urich, M.A., Chen, H., et al. (2015). Human body epigenome maps reveal noncanonical DNA methylation variation. Nature *523*, 212–216. https://doi.org/10.1038/nature14465.

90. Martin, M. (2011). Cutadapt removes adapter sequences from high-throughput sequencing reads. EMBnet J. *17*, 10–12. https://doi.org/10.14806/ej.17.1.200.

91. Langmead, B., and Salzberg, S.L. (2012). Fast gapped-read alignment with Bowtie 2. Nat. Methods *9*, 357–359. https://doi.org/10.1038/nmeth.1923.

92. Korotkevich, G., Sukhov, V., Budin, N., Shpak, B., Artyomov, M.N., and Sergushichev, A. (2016). Fast gene set enrichment analysis. Preprint at bioRxiv, 060012.

93. Zhang, Y., Liu, T., Meyer, C.A., Eeckhoute, J., Johnson, D.S., Bernstein, B.E., Nusbaum, C., Myers, R.M., Brown, M., Li, W., and Liu, X.S. (2008). Model-based analysis of ChIP-Seq (MACS). Genome Biol. *9*, R137. https://doi.org/10.1186/gb-2008-9-9-r137.

94. Robinson, M.D., McCarthy, D.J., and Smyth, G.K. (2010). edgeR: a Bioconductor package for differential expression analysis of digital gene expression data. Bioinformatics *26*, 139–140. https://doi.org/10.1093/bioinformatics/btp616.

95. Bolstad, B.M. and Bolstad, M.B.M. (2013). Package 'preprocessCore'. Bioconductor.

96. Schep, A.N., Wu, B., Buenrostro, J.D., and Greenleaf, W.J. (2017). chromVAR: inferring transcription-factor-associated accessibility from single-cell epigenomic data. Nat. Methods *14*, 975–978. https://doi.org/10.1038/nmeth.4401.

97. Grant, C.E., Bailey, T.L., and Noble, W.S. (2011). FIMO: scanning for occurrences of a given motif. Bioinformatics *27*, 1017–1018. https://doi.org/10.1093/bioinformatics/btr064.

98. Welch, J.D., Kozareva, V., Ferreira, A., Vanderburg, C., Martin, C., and Macosko, E.Z. (2019). Single-Cell Multi-omic Integration Compares and Contrasts Features of Brain Cell Identity. Cell *177*, 1873–1887.e17. https://doi.org/10.1016/j.cell.2019.05.006.

99. Quinlan, A.R., and Hall, I.M. (2010). BEDTools: a flexible suite of utilities for comparing genomic features. Bioinformatics *26*, 841–842. https://doi.org/10.1093/bioinformatics/btq033.

100. Roy Choudhury, S., Johns, S.M., and Pandey, S. (2019). A convenient, soil-free method for the production of root nodules in soybean to study the effects of exogenous additives. Plant Direct *3*, e00135. https://doi.org/10.1002/pld3.135.

101. Pelletier, J.M., Kwong, R.W., Park, S., Le, B.H., Baden, R., Cagliari, A., Hashimoto, M., Munoz, M.D., Fischer, R.L., Goldberg, R.B., and Harada, J.J. (2017). LEC1 sequentially regulates the transcription of genes involved in diverse developmental processes during seed development. Proc. Natl. Acad. Sci. USA *114*, E6710–E6719. https://doi.org/10.1073/pnas.1707957114.

102. Urich, M.A., Nery, J.R., Lister, R., Schmitz, R.J., and Ecker, J.R. (2015). MethylC-seq library preparation for base-resolution whole-genome bisulfite sequencing. Nat. Protoc. *10*, 475–483. https://doi.org/10.1038/nprot.2014.114.

103. Valliyodan, B., Cannon, S.B., Bayer, P.E., Shu, S., Brown, A.V., Ren, L., Jenkins, J., Chung, C.Y.L., Chan, T.F., Daum, C.G., et al. (2019). Construction and comparison of three reference-quality genome assemblies for soybean. Plant J. *100*, 1066–1082. https://doi.org/10.1111/tpj.14500.

104. Korsunsky, I., Millard, N., Fan, J., Slowikowski, K., Zhang, F., Wei, K., Baglaenko, Y., Brenner, M., Loh, P.R., and Raychaudhuri, S. (2019). Fast, sensitive and accurate integration of single-cell data with Harmony. Nat. Methods *16*, 1289–1296. https://doi.org/10.1038/s41592-019-0619-0.

105. Zhang, Y., Jang, H., Luo, Z., Dong, Y., Xu, Y., Kantamneni, Y., and Schmitz, R.J. (2024). Dynamic evolution of the heterochromatin sensing histone demethylase IBM1. PLoS Genet. *20*, e1011358. https://doi.org/10.1371/journal.pgen.1011358.

106. Stuart, T., Butler, A., Hoffman, P., Hafemeister, C., Papalexi, E., Mauck, W.M., 3rd, Hao, Y., Stoeckius, M., Smibert, P., and Satija, R. (2019). Comprehensive integration of single-cell data. Cell *177*, 1888–1902.e21. https://doi.org/10.1016/j.cell.2019.05.031.

107. Thomas, P.D., Ebert, D., Muruganujan, A., Mushayahama, T., Albou, L.P., and Mi, H. (2022). PANTHER: making genome-scale phylogenetics accessible to all. Protein Sci. *31*, 8–22. https://doi.org/10.1002/pro.4218.

108. Domcke, S., Hill, A.J., Daza, R.M., Cao, J., O'Day, D.R., Pliner, H.A., Aldinger, K.A., Pokholok, D., Zhang, F., Milbank, J.H., et al. (2020). A human cell atlas of fetal chromatin accessibility. Science *370*, eaba7612. https://doi.org/10.1126/science.aba7612.

109. Qiao, X., Li, Q., Yin, H., Qi, K., Li, L., Wang, R., Zhang, S., and Paterson, A.H. (2019). Gene duplication and evolution in recurring polyploidization-diploidization cycles in plants. Genome Biol. *20*, 38. https://doi.org/10.1186/s13059-019-1650-2.

110. Grant, C.E., and Bailey, T.L. (2021). XSTREME: Comprehensive motif analysis of biological sequence datasets. Preprint at bioRxiv.

111. Hao, Y., Stuart, T., Kowalski, M.H., Choudhary, S., Hoffman, P., Hartman, A., Srivastava, A., Molla, G., Madad, S., Fernandez-Granda, C., and Satija, R. (2024). Dictionary learning for integrative, multimodal and scalable single-cell analysis. Nat. Biotechnol. *42*, 293–304. https://doi.org/10.1038/s41587-023-01767-y.

STAR★METHODS

KEY RESOURCES TABLE

REAGENT or RESOURCE	SOURCE	IDENTIFIER
Bacterial and virus strains		
Bradyrhizobium japonicum strain	Dr. Jianxin Ma	USDA110
Critical commercial assays		
Chromium Next GEM Single Cell ATAC Library and Gel Bead Kit v1.1	10X Genomics	PN-1000175
Chromium Next GEM Single Cell 3' Kit v3.1	10X Genomics	PN-1000268
Visium Spatial Tissue Optimization Slide & Reagent Kit	10X Genomics	PN-1000193
Visium Spatial Gene Expression Slide & Reagent Kit	10X Genomics	PN-1000184
Deposited data		
Raw and analyzed data	This paper	GSE270392
Soybean GmHapMap SNPs	Torkamaneh et al.[34]	https://figshare.com/projects/Soybean_Haplotype_Map_GmHapMap_A_Universal_Resource_for_Soybean_Translational_and_Functional_Genomics/56921
RNA-seq for soybean seeds Laser Capture Microdissection (LCM)	http://seedgenenetwork.net/	GSE57349; GSE57350; GSE57606; GSE46906
Experimental models: Organisms/strains		
Soybean: Williams 82	USDA National Plant Germplasm System	Williams 82
Software and algorithms		
cellranger-atac (v1.2.0)	CellRanger ATAC (10X Genomics)	https://support.10xgenomics.com/single-cell-atac/software/pipelines/latest/what-is-cell-ranger-atac
Samtools v1.6	Danecek et al.[87]	http://www.htslib.org/download/
Picardtools v2.16	https://broadinstitute.github.io/picard/	https://broadinstitute.github.io/picard/
Socrates	Marand et al.[19]	https://github.com/plantformatics/Socrates
STARSolo	Blibaum et al.[88]	https://github.com/alexdobin/STAR/blob/master/docs/STARsolo.md
Seurat v4	Hao et al.[26]	https://satijalab.org/seurat/
Space Ranger	10X Genomics	https://www.10xgenomics.com/cn/support/software/space-ranger/latest
Methylpy	Schultz et al.[89]	https://github.com/yupenghe/methylpy
Cutadapt v2.8	Martin[90]	https://cutadapt.readthedocs.io/en/stable/
Bowtie 2.2.4	Langmead and Salzberg[91]	https://bowtie-bio.sourceforge.net/bowtie2/index.shtml
fgsea	Korotkevich et al.[92]	https://bioconductor.org/packages/release/bioc/html/fgsea.html
MACS2	Zhang et al.[93]	https://github.com/macs3-project/MACS
edgeR	Robinson et al.[94]	https://bioconductor.org/packages/release/bioc/html/edgeR.html
preprocessCore (v1.57.1)	Bolstad and Bolstad[95]	https://www.bioconductor.org/packages/release/bioc/html/preprocessCore.html
chromVAR	Schep et al.[96]	https://github.com/GreenleafLab/chromVAR
MEME	Grant et al.[97]	https://meme-suite.org/meme/
LIGER	Welch et al.[98]	https://github.com/welch-lab/liger
BEDtools	Quinlan and Hall[99]	https://bedtools.readthedocs.io/en/latest/
Analysis code	This paper	https://github.com/schmitzlab/soybean_atlas

EXPERIMENTAL MODEL AND STUDY PARTICIPANT DETAILS

Growth conditions

The soybean seeds of the Williams 82 genotype were obtained from the USDA National Plant Germplasm System (https://npgsweb.ars-grin.gov) and sown in Sungro Horticulture professional growing mix (Sungro Horticulture Canada Ltd.). For libraries derived from leaf, hypocotyl, nodule, and seed-related tissues, the plants were grown in a greenhouse under a 50/50 mixture of 4100K (Sylvania Supersaver Cool White Deluxe F34CWX/SS, 34W) and 3000K (GE Ecolux with Starcoat, F40CX30ECO, 40W) lighting, with a photoperiod of 16 hours of light and 8 hours of dark. The temperature was maintained at approximately 25°C during light hours, with a relative humidity of approximately 54%.

Soybean leaves

For each sample, approximately 6 leaves with a 1 cm diameter were harvested between 8 and 9 AM, ten days after sowing. Fresh tissue was used to construct bulk ATAC-seq (2 replicates), scATAC-seq (2 replicates) libraries.

Soybean hypocotyls

For each sample, approximately 4 hypocotyls were harvested between 8 and 9 AM, seven days after sowing. Fresh tissue was used to construct scATAC-seq (3 replicates) and snRNA-seq (2 replicates) libraries.

Soybean roots

Soybean root samples were obtained as follows: soybean seeds were sterilized with 70% ethanol for 1 minute. After removing the ethanol solution, the seeds were treated with 10% bleach for 5 minutes, followed by five washes with autoclaved Milli-Q water. The sterilized seeds were then sown on mesh plates with half-strength MS media (Phytotech Laboratories, catalog: M519) and wrapped in Millipore tape. Plates were incubated in a Percival growth chamber with a photoperiod of 16 hours of light and 8 hours of dark. The growth chamber temperature was set to 25°C with a relative humidity of approximately 60%. For each sample, approximately 5 whole roots were harvested between 8 and 9 AM, seven days after sowing. Fresh tissue was used to construct scATAC-seq (5 replicates) and snRNA-seq (2 replicates) libraries.

Soybean nodules

Soybean nodules were induced following a previously described soil-free method for producing root nodules in soybean.[100] Briefly, seeds were germinated in sterilized germination paper (Anchor Paper Company, St Paul, MN, USA) wetted with autoclaved water for 10 days. The roots were then infected with *Bradyrhizobium japonicum* strain USDA110 to produce nodules. Roots with nodules approximately 1 mm in diameter were collected 15 days post-inoculation (dpi), and root tips were removed (Figure 4F). The tissue was flash-frozen in liquid nitrogen and stored at -80°C. For each sample, approximately 10 tissues were used for scATAC-seq (3 replicates) and snRNA-seq (2 replicates) preparation.

Soybean pods

For each sample, approximately 20 whole pods, each 5 mm in length, were harvested between 8 and 9 AM in the greenhouse. Fresh tissue was used to construct scATAC-seq (4 replicates) libraries.

Soybean seeds

Seed stages were determined according to previously described methods and standards.[101] Specifically, seed lengths for the globular, heart, cotyledon, and early maturation stages were 1.0 mm, 2 mm, 3 mm, and 7 mm, respectively. Seeds at the middle maturation stage weighed about 200-250 mg. Fresh tissue was used to construct scATAC-seq and snRNA-seq libraries for all seed tissues. For scATAC-seq, four biological replicates were performed for globular stage seeds, while two biological replicates were conducted for the other tissues.

METHOD DETAILS

scATAC-seq library preparation

Nuclei isolation and purification were performed as described previously.[5] Briefly, the tissue was finely chopped on ice for approximately 2 minutes using 600 μL of pre-chilled Nuclei Isolation Buffer (NIB: 10 mM MES-KOH at pH 5.4, 10 mM NaCl, 250 mM sucrose, 0.1 mM spermine, 0.5 mM spermidine, 1 mM DTT, 1% BSA, and 0.5% Triton X-100). After chopping, the mixture was passed through a 40-μm cell strainer and centrifuged at 500 rcf for 5 minutes at 4°C. The supernatant was carefully decanted, and the pellet was reconstituted in 500 μL of NIB wash buffer (10 mM MES-KOH at pH 5.4, 10 mM NaCl, 250 mM sucrose, 0.1 mM spermine, 0.5 mM spermidine, 1 mM DTT, and 1% BSA). The sample was filtered through a 10-μm cell strainer and gently layered onto 1 mL of 35% Percoll buffer (35% Percoll mixed with 65% NIB wash buffer) in a 1.5-mL centrifuge tube. The nuclei were centrifuged at 500 rcf for 10 minutes at 4°C. After centrifugation, the supernatant was carefully removed, and the pellets were resuspended in 10 μL of diluted nuclei buffer (DNB, 10X Genomics Cat# 2000207). Approximately 5 μL of nuclei were diluted tenfold, stained with

DAPI (Sigma Cat. D9542), and the nuclei quality and density were evaluated using a hemocytometer under a microscope. The original nuclei were then diluted with DNB buffer to a final concentration of 3,200 nuclei per μL. Finally, 5 μL of nuclei (16,000 nuclei in total) were used as input for scATAC-seq library preparation.

scATAC-seq libraries were prepared using the Chromium scATAC v1.1 (Next GEM) kit from 10X Genomics (Cat# 1000175), following the manufacturer's instructions (10x Genomics, CG000209_Chromium_NextGEM_SingleCell_ATAC_ReagentKits_v1.1_UserGuide_RevE). Libraries were sequenced on an Illumina NovaSeq 6000 in dual-index mode with eight and 16 cycles for i7 and i5 indexes, respectively.

Bulk ATAC-seq library preparation

Nuclei isolation followed the exact procedure used for scATAC-seq, and the library preparation strictly adhered to the protocol described previously.[44]

snRNA-seq library preparation

The protocol for nuclei isolation and purification was adapted from a previously described scATAC-seq method. To minimize RNA degradation and leakage, the tissue was finely chopped on ice for approximately 1 minute using 600 μL of pre-chilled Nuclei Isolation Buffer containing 0.4 U/μL RNase inhibitor (Roche, Protector RNase Inhibitor, Cat. RNAINH-RO) and a low detergent concentration of 0.1% NP-40. Following chopping, the mixture was passed through a 40-μm cell strainer and centrifuged at 500 rcf for 5 minutes at 4°C. The supernatant was carefully decanted, and the pellet was reconstituted in 500 μL of NIB wash buffer (10 mM MES-KOH at pH 5.4, 10 mM NaCl, 250 mM sucrose, 0.5% BSA, and 0.2 U/μL RNase inhibitor). The sample was filtered again through a 10-μm cell strainer and gently layered onto 1 mL of 35% Percoll buffer (prepared by mixing 35% Percoll with 65% NIB wash buffer) in a 1.5-mL centrifuge tube. The nuclei were centrifuged at 500 rcf for 10 minutes at 4°C. After centrifugation, the supernatant was carefully removed, and the pellets were resuspended in 50 μL of NIB wash buffer. Approximately 5 μL of nuclei were diluted tenfold and stained with DAPI (Sigma Cat. D9542). The quality and density of the nuclei were evaluated using a hemocytometer under a microscope. The original nuclei were further diluted with DNB buffer to achieve a final concentration of 1,000 nuclei per μL. Ultimately, a total of 16,000 nuclei were used as input for snRNA-seq library preparation.

For scRNA-seq library preparation, we employed the Chromium Next GEM Single Cell 3'GEM Kit v3.1 from 10X Genomics (Cat# PN-1000123), following the manufacturer's instructions (10xGenomics, CG000315_ChromiumNextGEMSingleCell3-_GeneExpression_v3.1_DualIndex_RevB). The libraries were subsequently sequenced using the Illumina NovaSeq 6000 in dual-index mode with 10 cycles for the i7 and i5 indices, respectively.

Spatial RNA-seq library preparation

For the spatial RNA-seq experiment, the hypocotyl tissues, the root tissues, and the seed tissues at the heart stage, cotyledon stage, and early maturation stage, matching the stages of the single-cell datasets, were sampled. The tissues were embedded in the Optimal Cutting Temperature (OCT) compound, snap-frozen in a cold 2-methylbutane bath merged in liquid nitrogen, and cryosectioned into 12 um thick slices.

We used the Visium Spatial Gene Expression Kit (10X Genomics, USA) to construct the spatial RNA-seq libraries following the manufacturer's instructions. The tissue sections were mounted onto the spatial slides, fixed by cold methanol, and stained by 0.05% toluidine blue. The stained tissue sections were imaged using the BZ-X800 fluorescent microscope (Keyence, Japan). To determine the optimal tissue permeabilization time, we performed the Tissue Optimization workflow on a series of digestion times for each tissue type. For the spatial RNA-seq libraries, mRNA was first released according to the optimal permeabilization time, then the spatially barcoded cDNAs were synthesized on the slides. Finally, cDNA were released from the slide and subjected to amplification and library construction, following the manufacturer's specifications

Library preparation of whole genome bisulfite sequencing

Libraries were constructed following the MethylC-seq protocol.[102] In summary, genomic DNA was isolated from the endosperm tissues (early maturation stage) using the DNeasy Plant Mini Kit (Qiagen). The extracted DNA was then subjected to sonication to generate fragments of approximately 200 bp. End repair was carried out using the End-It DNA End-Repair Kit (Epicentre). The resulting end-repaired DNA underwent A-tailing with the Klenow 3′–5′ exo− enzyme (New England Biolabs). Methylated adapters were subsequently ligated to the A-tailed DNA using T4 DNA Ligase (New England Biolabs). Following ligation, the DNA underwent bisulfite conversion with the EZ DNA Methylation-Gold Kit. Finally, the library was amplified using KAPA HiFi Uracil + Readymix Polymerase (Roche).

QUANTIFICATION AND STATISTICAL ANALYSIS

scATAC-seq raw reads processing

The raw data processing followed the previously described method.[19] In brief, raw BCL files were demultiplexed and converted into fastq format using the default settings of the 10X Genomics tool cellranger-atac makefastq (v1.2.0). Initial read processing, including adaptor/quality trimming, mapping, and barcode attachment/correction, was carried out with cellranger-atac count (v1.2.0) using the

soybean Williams 82 v4 reference genome and the Glycine max organelle genomes (NCBI Reference Sequence: NC_007942.1, NC_020455.1).[103] Properly paired mapped reads with a mapping quality greater than 30 were retained using samtools view (v1.6; -f 3 -q 30),[88] while also retaining reads with alternate hit XA tags to avoid biasing downstream analysis due to the whole genome duplication events during soybean evolution. Duplicate fragments were collapsed on a per-nucleus basis using picardtools (http://broadinstitute.github.io/picard/) MarkDuplicates (v2.16; BARCODE_TAG=CB REMOVE_DUPLICATES=TRUE). Reads mapping to mitochondrial and chloroplast genomes were counted for each barcode and then excluded from downstream analysis. Potential artifacts were removed by excluding alignments coinciding with a blacklist of regions exhibiting Tn5 integration bias from Tn5-treated genomic DNA (1-kb windows with greater than 4x coverage over the genome-wide median) and potential collapsed sequences in the reference (1-kb windows with greater than 4x coverage over the genome-wide median using ChIP-seq input). BAM alignments were then converted to single base-pair Tn5 integration sites in BED format by adjusting coordinates of reads mapping to positive and negative strands by +4 and -5, respectively, and retaining only distinct Tn5 integration sites for each individual barcode.

The R package Socrates was used for nuclei identification and quality control.[19] The BED file containing single base-pair Tn5 integration sites was imported into Socrates along with the soybean GFF gene annotation (Phytozome, version Gmax_508_Wm82.a4.v1) and the genome index file. To identify bulk-scale ACRs in Socrates, the callACRs function was employed with the following parameters: genome size=8.0e8, shift=-75, extsize=150, and FDR=0.1. This step allowed us to estimate the fraction of Tn5 integration sites located within ACRs for each nucleus. Metadata for each nucleus were collected using the buildMetaData function, with a TSS (Transcription Start Site) window size of 1 kb (tss.window=1000). Sparse matrices were then generated with the generateMatrix function, using a window size of 500. High-quality nuclei were identified based on the following criteria: a minimum of 1,000 Tn5 insertion sites per nucleus, at least 20% of Tn5 insertions within 2 kb of TSSs, and at least 20% of Tn5 insertions within ACRs across all datasets. Additionally, a maximum of 20% of Tn5 insertions in organelle genomes was allowed.

For each tissue, integrated clustering analysis of all replicates was performed using the R package Socrates.[19] For the binary nucleus x window matrix, windows accessible in less than 1% of all nuclei and nuclei with fewer than 100 accessible ACRs were removed using the function cleanData (min.c=100, min.t=0.01). The filtered nucleus x window matrix was normalized with the term-frequency inverse-document-frequency (TF-IDF) algorithm with L2 normalization (doL2=T). The dimensionality of the normalized accessibility scores was reduced using the function reduceDims while removing singular values correlated with nuclei read depth (method="SVD", n.pcs=25, cor.max=0.4). The reduced embedding was visualized as a UMAP embedding using projectUMAP (k.near=15). Approximately 5% of potential cell doublets were identified and filtered by performing a modified version of the Socrates workflow on each library separately with the function detectDoublets and filterDoublets (filterRatio=1.0, removeDoublets=T). To address batch effects, we used the R package Harmony with non-default parameters (do_pca=F, vars_use=c("batch"), tau=5, lambda=0.1, nclust=50, max.iter.cluster=100, max.iter.harmony=50). The dimensionality of the nuclei embedding was further reduced with Uniform Manifold Approximation Projection (UMAP) via the R implementation of projectUMAP (metric="correlation", k.near=15). Finally, the nuclei were clustered with the function callClusters (res=0.5, k.near=15, cl.method=3, m.clust=25).

snRNA-seq raw reads processing

STARSolo was used to map the snRNA-seq reads and count the gene features using the soybean genome (William 82 v4).[87] We specified the following parameters in *STARSolo* to filter the UMI, filter empty cells, and count multi-mapping reads: –soloUMIfiltering MultiGeneUMI_CR, –soloCellFilter EmptyDrops_CR, –soloMultiMappers PropUnique. This ensures that non-uniquely mapped multigene UMIs are distributed uniformly among multi-mapped loci. The filtered expression data was analyzed using the *Seurat* (v4) R package.[26] Potential low-quality nuclei or empty droplets were filtered. Specifically, cells with gene counts below a threshold calculated as the median gene count minus two times the median absolute deviation, and cells with UMI counts less than the lower 10% percentile of total UMI counts, were filtered out. Additionally, cells with organelle gene counts comprising more than 15% of the total gene count were excluded. Due to substantial contamination from chloroplast-derived reads in leaf and insufficient UMI counts in pod and MMS seed, these tissues were excluded from further analyses. The preprocessed datasets were normalized using *SCTransform* before the *RunPCA* for principal component analysis (PCA). Subsequently, the doublets were identified by the *DoubletFinder* R package, and removed from downstream analysis. We prepared two replicates for each library and integrated them using the *Harmony* R package.[104] The integrated dataset was then processed using *RunUMAP* (reduction = "harmony", dims = 1:20) for Uniform Manifold Approximation and Projection (UMAP) dimension reduction, *FindNeighbors* (reduction = "harmony", dims = 1:30) to obtain the Nearest-neighbor graph, and *FindClusters* to identify distinct cell populations. Different resolutions were selected to classify cell types in varying tissue types. We used *FindSubCluster* to identify the sub-clusters according to the specificity of marker genes.

spRNA-seq reads processing

We used Space Ranger (10X Genomics) to map the spRNA-seq reads to the soybean genome and to count gene expression. The filtered gene expression matrix was analyzed using the *Seurat* (v4) R package.[26] All the datasets were analyzed using *SCTransform* and *RunPCA*. To remove the batch effect for replicates placed in different spatial capture areas, we used the *Harmony* R package to integrate the replicates and analyzed it using *RunUMAP* (reduction = "harmony", dims = 1:20) and *FindNeighbors* (reduction = "harmony", dims = 1:20). We used *FindClusters* to identify cell clusters and *FindSubCluster* to identify the subclusters for specific cell types. Various resolutions were used to identify the cell clusters in distinct types of tissues.

DNA methylation analysis

WGBS data were analyzed using Methylpy,[89] in accordance with the procedure outlined in reference[105]. Initially, reads were trimmed using Cutadapt v2.8.[90] The filtered reads were then aligned to the soybean reference genome (Gmax_508_v4.0) with Bowtie 2.2.4,[91] ensuring that only uniquely aligned and non-clonal reads were retained. The non-conversion rate of unmodified cytosines during the sodium bisulfite treatment was assessed using a chloroplast genome as a control for sequences that are fully unmethylated. Density plots were generated based on the calculated methylation differences across 50 bp windows, which included at least 20 informative sequenced cytosines in both samples, along with a minimum of 70% CG, 50% CHG, or 10% CHH methylation in either of the samples.

Integration of snRNA-seq and spRNA-seq

We applied the 'anchor'-based integration method from *Seurat* to integrate the snRNA-seq and spRNA-seq datasets.[106] First, we used *FindTransferAnchors* (normalization.method="SCT") to find the anchors between the reference dataset (snRNA-seq) and the query dataset (spRNA-seq). These anchors were used to calculate the prediction scores of each snRNA-seq cell type for the spRNA-seq using the *TransferData* (dims = 1:30).

De novo marker identification

After cell type annotation, we identified the *de novo* marker genes using the *FindAllMarkers* (test.use="wilcox", logfc.threshold = 1, only pos=T, min.pct = 0.1) from the *Seurat* R package. Then we took the top 50 most up-regulated genes and filtered them by adjusted p-value>0.00001 and $\log_2$FC>2 to obtain the significant marker genes.

Cell-type annotation for snRNA-seq

To assign cell types to each cluster, we used a combination of marker gene-based annotation and gene set enrichment analysis. Initially, we compiled a list of known cell-type-specific marker genes known to localize to discrete cell types or domains expected in the sampled tissues based on an extensive review of the literature (Table S2). The putative ortholog list for *Arabidopsis* and soybean was downloaded from PANTHER (v18.0).[107] We considered the least diverged ortholog (LDO) genes inferred by PANTHER, which are most likely to retain the greatest functional similarities, as the representative orthologs. Gene expression was calculated using the UMI counts in the gene body and aggregating all nuclei in a cluster, then the raw counts matrix was normalized with the CPM function in edgeR. The *Z*-score was calculated for each marker gene across all cell types using the scale function in R, and key cell types were assigned based on the most enriched marker genes with the highest *Z*-score. Ambiguous clusters displaying similar patterns to key cell types were assigned to the same cell type as the key cell types, reflecting potential variations in cell states within a cell type (Figure S2). To aid visualization, we smoothed normalized gene accessibility scores by estimating a diffusion nearest neighbor graph.[19]

For soybean seed tissue, the cpm normalized matrix was also mapped to the subregion by checking the correlation with the laser capture microdissection (LCM) RNA-seq dataset (http://seedgenenetwork.net/seeds). With this approach, we could clearly identify the seed coat, endosperm, and embryo regions, which confirmed our cell type annotation. There were no available markers for seed coat endothelium and seed coat inner integument, so these two cell types were annotated based on specific high correlations with the LCM dataset (Figures S1M and S1N).

For gene set enrichment analysis, we used the R package fgsea, following a methodology described previously.[19,92] Firstly, we constructed a reference panel by uniformly sampling nuclei from each cluster, with the total number of reference nuclei set to the average number of nuclei per cluster. Subsequently, we aggregated the UMI counts across nuclei in each cluster for each gene and identified the differential expression profiles for all genes between each cluster and the reference panel using the R package edgeR.[94] For each cluster, we generated a gene list sorted in decreasing order of the $\log_2$ fold-change value compared to the reference panel and utilized this list for gene set enrichment analysis. We excluded GO terms with gene sets comprising less than 10 or greater than 600 genes from the analysis, and GO terms were considered significantly enriched at an FDR < 0.05 with 10,000 permutations. The cell type annotation was additionally validated by identifying the top enriched GO terms that align with the expected cell type functions.

Cell-type annotation for scATAC-seq

A similar approach used for snRNA-seq cell type annotation was applied to scATAC-seq with minor optimizations. Specifically, the gene chromatin accessibility score, rather than gene expression, was calculated using the Tn5 integration number in the gene body, a 500 bp upstream region, and a 100 bp downstream region. The raw counts were then normalized with the cpm function in edgeR. Cell types were assigned to each cluster following the snRNA-seq annotation process, including evaluating marker gene performance and GO enrichment profiles.

For tissues with both snRNA-seq and scATAC-seq data, we further confirmed the cell annotations by integrating the two modalities using the *Seurat* workflow (v4.0.4).[26] Briefly, the gene chromatin accessibility score was normalized and scaled with the functions NormalizeData and ScaleData. The function FindTransferAnchors was used for canonical correlation analysis (CCA) to compare the scATAC-seq gene score matrix with the scRNA-seq gene expression matrix and to find mutual nearest neighbors in low-dimensional space. Annotations from the scRNA-seq dataset were then transferred onto the scATAC-seq cells using the TransferData function, and prediction scores less than 0.5 were filtered out. This approach allowed us to match and validate cell types across

the two modalities, and we observed a median prediction score of 0.75 across the seven tissues (Figures S1O–S1Q). Finally, we calculated the Pearson correlation coefficient with the top 1,000 variable genes from snRNA-seq, which ranged from 0.4 to 0.7 for the same cell type across the two modalities, similar to observations from other studies (Figures S2M–S2P).[19,70,108]

ACR identification

Following cell clustering and annotation, peaks were identified using all Tn5 integration sites for each cluster by running MACS2 with non-default parameters: –extsize 150 –shift -75 –nomodel –keep-dup all.[93] To account for potential bias introduced by read depth, we adjusted the q-value cutoffs based on the total Tn5 integration number in each cell type as follows: for less than 10 million integrations, we used –qvalue 0.1; for 10-25 million, we used 0.05; for 25-50 million, we used 0.025; for 50-100 million, we used 0.01; and for more than 100 million, we used 0.001. Peaks were then redefined as 500-bp windows centered on the peak coverage summit. To consolidate information across all clusters, we concatenated all peaks into a unified master list using a custom script.[19] The peak chromatin accessibility score was calculated based on the Tn5 integration count within the peak and then normalized using the cpm function in edgeR.[94] ACRs with less than 4 CPM in all cell types were removed from downstream analysis. We also used the same method described above to identify the ACRs for bulk ATAC-seq data.

Predicting the functions of ACRs

We hypothesized that the ACRs only control the flanking genes and used a correlation-based approach to predict the function of the ACRs. Firstly, we created the count matrix of the ACRs and gene expression across 66 main shared cell types between scATAC-seq and snRNA-seq. The count matrix was then normalized using the cpm function in edgeR and the normalize.quantiles function in preprocessCore (v1.57.1).[95] For each test, we calculated the Spearman correlation between the ACRs accessibility and gene expression, shuffling the ACRs accessibility and gene expression 1,000 times to obtain a p-value for each correlation. This allowed us to compute the p-value for each correlation and adjust for multiple hypotheses using the Benjamini-Hochberg procedure (FDR). We then selected all correlations below -0.25 and above 0.25 with an FDR below 0.05. To simplify the ACRs function, we hypothesized that one ACR controls one gene. To simplify the characterization of ACR function, we hypothesized that one ACR controls one gene. For ACRs associated with multiple genes, we filtered the associations based on the following ACR-gene distance criteria: (i) Keep the association with the highest correlation if all the associations were genic and proximal to the focal gene. (ii) Keep the association with the highest correlation if all the associations were distal to the focal gene. (iii) If the associations were a mix of distal, genic, or proximal, we retained the distal association with the highest correlation, along with the genic or proximal association. Finally, the ACRs with all positive correlations with a flanking gene were predicted as activating ACRs, and the ACRs with all negative correlations with a flanking gene were predicted as repressing ACRs. About 3.9% of ACRs had both negative and positive correlations with a flanking gene, and these ACRs with ambiguous functions were removed from downstream analysis.

Identification of whole genome duplication ACRs

The whole genome duplication ACRs were identified using established methods.[36] Briefly, whole genome duplication genes were detected through *DupGene_finder* pipelines.[109] ACRs from duplicated gene pairs were aligned, and if the e-value was less than 0.01, the ACR pair was classified as duplicated ACR pairs.

Identification of intergenic negative control regions

The intergenic negative control regions were constructed following the reported methods.[45] Briefly, we first filtered all genome coordinates to retain only uniquely mappable regions, and then subtracted annotated genes and their 2 kb flanking regions, as well as ACRs apart of gene-ACR pairs identified by our analyses. The negative control regions with the same number and length distribution of observed ACRs were then generated by the "shuffle" command in BEDTools.[99]

Identification of cell-type-specific ACRs

To identify the cell-type-specific ACRs, we first identified the differentially accessible chromatin regions for each cell type in the tissue. Specifically, for each cell type, we constructed a reference panel by uniformly sampling nuclei from other cell types, with the total number of reference nuclei set to the number of nuclei in the tested cell type. Subsequently, we aggregated the Tn5 integration counts across nuclei in the cell type for each replicate and identified the differential accessibility profiles for all ACRs between each cell type and their reference panel using the R package edgeR. High accessible ACRs in a cell type with a fold change > 4 and p-value < 0.05 were aggregated in the tissue. ACRs identified as highly accessible in at most two cell types were retained as cell-type-specific ACRs in the tissue.

TF Motif deviations score calculation

TF motif deviation scores of specific TF motifs among nuclei were estimated using chromVAR[96] with the non-redundant core plant PWM database from JASPAR2022. The input matrix for chromVAR was filtered to retain ACRs with a minimum of 10 fragments and cells with at least 100 accessible ACRs. We applied smoothing to the bias-corrected motif deviations for each nucleus, integrating them into UMAP embedding for visualization, like the method used for visualizing gene body chromatin accessibility.

Motif enrichment

Firstly, TF motif occurrences in all ACRs were identified with fimo from the MEME suite toolset[47,97] using position weight matrices (PWM) from the non-redundant core plant motif database in JASPAR 2024. To test the motif enrichment in the cell-type-specific ACRs, we compared the motif distribution in the ctACRs and a control set of "constitutive" ACRs, which varied the least and were broadly accessible across cell types (fold change < 2 and p-value > 0.1), using Fisher's exact test (alternative = 'greater') for each cell type and motif. To control for multiple testing, we used the Benjamini-Hochberg method to estimate the FDR, considering tests with FDR < 0.05 as significantly different between the cell-type-specific ACRs and constitutively accessible regions. To test the motif enrichment in the activating ACRs and repressing ACRs, we compared the motif distribution in the activating ACRs and repressing ACRs using Fisher's exact test (alternative = 'greater') for each motif. Motifs with a p-value less than 0.01 were considered significantly enriched.

De novo TF motif enrichment

To identify potential unknown motifs in the cell-type-specific ACRs, we first created a control set by randomly selecting the same number of cell-type-specific ACRs from the "constitutive" ACRs described above, ensuring that they had a similar GC content ratio to the test set. De novo motif searches in cell-type-specific ACRs were performed using XSTREME version 5.5.3 within the MEME suite package (v5.5.0)[110] with the non-default parameter ''–maxw 30,'' and we provided the known motifs from the non-redundant core plant motif database in JASPAR 2024 or collected from the literature.

Embryo scATAC-seq and scRNA-seq clustering

To chart the dynamics of chromatin accessibility and transcription during embryogenesis, we first collected all scATAC-seq and snRNA-seq nuclei with embryo cell type annotations from the four matched seed developmental time points (Globular, Heart, Cotyledon, and Early Maturation stages), and re-clustered scATAC-seq and snRNA-seq nuclei, independently.

For the snRNA-seq data set, we first partitioned the nuclei x gene matrix corresponding specifically to embryo cell types and removed genes expressed in less than 0.1% of nuclei. To remove outlier nuclei, we then selected nuclei with at least 100 distinct expressed genes and less than 10,000 expressed genes. The sparse gene x nuclei matrix was then processed with the R package, *Seurat* (v5.0.1) by first log-normalizing counts using *NormalizeData* with default parameters.[111] We scaled the normalized counts with *ScaleData* and regressed out effects from variation in the log-scaled UMI counts and percent UMIs mapping to organeller genes. The scaled matrix was then used to identify variable features via *FindVariableFeatures* with non-default parameters (selection.method=''mean.var.plot'', dispersion.cutoff=c(0.5, Inf), mean.cutoff=c(0.0125,3)). To reduce the dimensionality of the nuclei x gene matrix, we ran principal component analysis with *RunPCA* to identify the top 20 PCs. The reduced embedding was used as input for UMAP from the *uwot* R package (min_dist=0.01, n_neighbors=30, metric=''cosine''). We then generated a neighborhood graph with *FindNeighbors* with non-default parameters (dims=1:20, nn.esp=0, k.param=30, annoy.metric=''cosine'', n.trees=100, prune.SNN=1/30, l2.norm=T). Finally, we identified clusters using the *FindClusters* function with resolution=1 and the leiden algorithm (algorithm=4). Cluster cell types were derived from the prior annotation strategy and validated using marker gene expression profiles from the new clustering results (Table S2).

To recluster the scATAC-seq embryo nuclei, we first partitioned the nuclei x ACR matrix specifically for nuclei labeled as embryo cell types from the prior annotation. All downstream scATAC-seq analyses were conducted inside the *Socrates* framework unless otherwise noted. Nuclei with less than 100 distinct accessible chromatin regions were removed and ACRs that were accessible in less than 1% of nuclei were also excluded using the function *cleanData* (min.c=100, min.t=0.01). The nuclei x ACR matrix was normalized by TFIDF followed by taking the L2 norm of each nucleus with the function *tfidf* and non-default parameters (doL2=T). To reduce the dimensionality of this matrix, we performed Singular Value Decomposition (SVD), taking the top 25 singular values after removing singular values correlated with per-nucleus read depths greater than 0.5, and L2 normalizing the components via non-default parameters of the function *reduceDims* (n.pcs=25, method=''SVD'', cor.max=0.5, scaleVar=T, doL2=T). The reduced matrix was then projected into two-dimensions with *projectUMAP* with non-default settings (metric=''cosine'', k.near=15). To identify clusters, we generated a shared neighborhood graph and clustered the data using leiden with the function *callClusters* with non-default parameters (res=0.5, k.near=15, cleanCluster=T, cl.method=4, e.thresh=3, m.clust=25, min.reads=5e5) to remove UMAP outliers and clusters with less than 25 nuclei and a total read depth of 500,000. Cell type annotations for each cluster were determined similarly as for the snRNA-seq clustering results.

Embryo scATAC-seq and snRNA-seq integration

To determine the best integration strategy for these data, we compared the preservation of local neighborhoods among scATAC-seq nuclei before and after integration with matched snRNA-seq data sets using Seurat (v4 integration),[26] and the NMF and uiNMF workflows from the R package, *liger*.[98] Our results indicated that uiNMF (accuracy=0.82) and NMF (accuracy=0.78) were the best approaches for predicting scATAC-seq nuclei cell identity using the snRNA-seq cell identity labels (i.e. agreement between independently ascertained scATAC-seq cell type labels and predicted labels based on similarity to snRNA-seq nuclei; Figure S6T). Although uiNMF outperformed the other methods, Seurat v4 integration still provided reasonably reliable cell type predictions (accuracy = 0.7; Figure S6T). Since uiNMF yielded the highest fraction of shared nearest neighbors between pre- and post-integration across all scATAC-seq nuclei, we used the uiNMF co-embedding for all downstream analyses. We describe the uiNMF integration procedure in greater detail below.

To perform the uiNMF integration, we first partitioned three matrices (nuclei x gene accessibility, nuclei x ACR, and nuclei x gene expression) to specifically retain embryo nuclei from the scATAC-seq and snRNA-seq clustering results from above. The integration was performed using the unshared features iNMF workflow from the R package, *liger*.[98] Importantly, this approach only uses gene body chromatin accessibility that exhibits positive correlative structure with gene expression during the non-negative matrix factorization step. The unshared features (ACRs) are only used to capture nuclei-nuclei relationships in the scATAC-seq data to preserve local neighborhoods in the co-embedding. Thus, repressive ACRs likely have a minimal to non-existent contribution to the co-embedding. Specifically, we normalized the nuclei x ACR matrix by *tfidf* (*Socrates*) followed by the *normalize* function of *liger* with default settings. The normalized nuclei x ACR slot was then rescaled such that the sum of all accessible regions for a given barcode was 1. Using the *Seurat* framework, we then identified the top 2,000 most variable features using *FindVariableFeatures* with non-default parameters (selection.method="vst", nfeatures=2000). The normalized nuclei x ACR matrix was scaled using *scaleNotCenter* and stored as the set of unshared features for downstream integration.

Focusing on the matrices with the shared feature set (geneIDs) between scATAC-seq and snRNA-seq, we selected genes from each modality within the inner 98% quantile of each distribution and retained the intersected genes. The nuclei x gene activity and nuclei x gene expression matrices were normalized using the default settings of the *normalize* function. Variable genes were selected using *selectGenes* with var.thresh=0.1, datasets.use="RNA", unshared=TRUE, unshared.datasets=list(2), unshared.thresh=0.2 parameters. The normalized matrices were scaled with *scaleNotCenter* with default settings. The integration was performed with the function *optimizeALS* by setting k=30, use.unshared=TRUE, max_iters=30, and thresh=1e-10. Finally, the integrated embedding was quantile normalized with the function *quantile_norm* setting the reference data set to the snRNA-seq modality.

Using the integrated embedding based on the snRNA-seq nuclei as a reference, we then aimed to impute scATAC-seq modalities on to the snRNA-seq nuclei. To accomplish this, we ran the function *imputeKNN* from the *liger* package to impute motif deviation scores and ACR normalized chromatin accessibility values from the scATAC-seq nuclei onto the snRNA-seq nuclei using default parameters. This results in estimates of gene expression, chromatin accessibility, and motif deviation scores for an individual snRNA-seq barcode.

Inferred developmental age of embryo nuclei

The time-series nature of the four seed developmental stages of our data lends itself to precise inference of developmental age using model-based approaches.[70] To simplify interpretation, we focused on the snRNA-seq embryo nuclei across the four developmental stages. Starting from the raw nuclei x gene counts matrix, we log-transformed counts and scaled the resulting values such that the sum across all genes was equal to 10,000 for each barcode. We then downsampled each stage to have the same number of nuclei. Using the R package, *caret*, we partitioned the downsampled nuclei into training and test sets via the function *createDataPartition* with non-default parameters (seed_stage, p=10/11, list=F, times=1). We then trained a linear regression model with a LASSO penalty and 10-fold cross-validation using the *cv.glmnet* function from the R package, *glmnet*, on gene expression profiles for seed stage. The model was then used to collect gene coefficients and continuous developmental age predictions from the entire data set.

Trajectory analysis

Pseudotime trajectory analysis for each trajectory outlined in Figures 5H, 5I, and 6E was performed similar to a previously published approach.[19] Specifically, we ran the function *calcPseudo* with cell.dist1=0.95 and cell.dist2=0.95 from the github repository (https://github.com/plantformatics/maize_single_cell_cis_regulatory_atlas), resulting in pseudotime estimates for individual nuclei for a specific developmental branch. We then identified genes with significant gene expression variation across each trajectory using the function *sigPseudo2* from the same github repo. For visualization, gene expression scores across pseudotime for significantly variable genes were smoothed using predictions on 500 equally spaced bins from a generalized additive model as previously shown.[19]

To identify TFs associated with gene expression variation across pseudotime during Cotyledon parenchyma development, we performed a Pearson's correlation analysis between TF motif deviations and genes with significant pseudotime variance. TF modules were clustered using k-means, where the final k=8 was selected based on the elbow and silhouette approaches.

CellPress

Supplemental figures

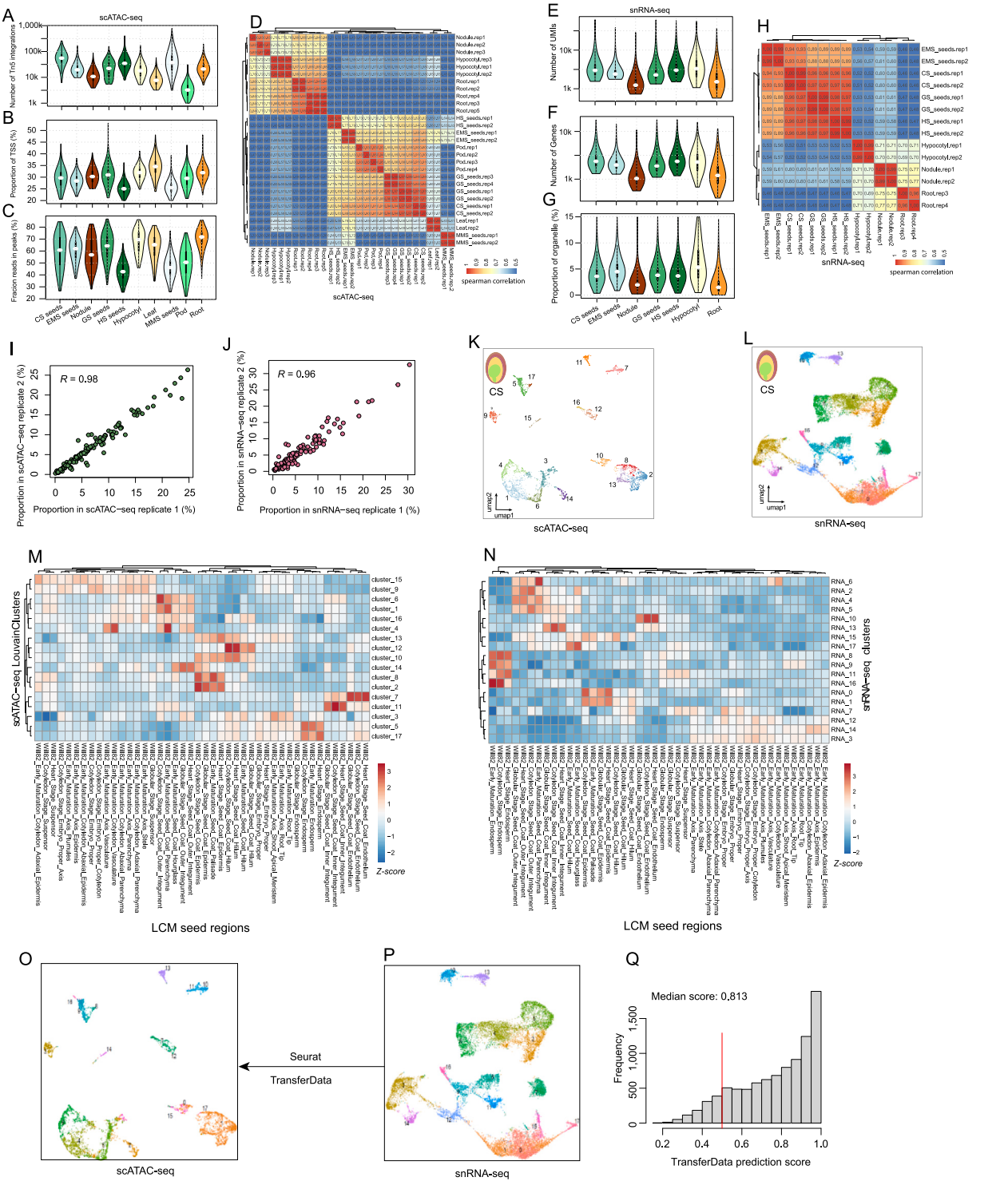

(legend on next page)

Figure S1. Evaluation and quality control of soybean scATAC-seq and snRNA-seq, related to Figure 1

(A–D) Quality control of scATAC-seq: distribution of Tn5 integration sites per nucleus across ten tissues (A); distributions of the proportion of Tn5 integration sites within the promoter regions, encompassing the 1-kb flanking regions around gene transcription start sites (TSSs) (B); distributions of the proportion of Tn5 integration sites within peaks per nucleus (C); and Spearman's correlation coefficient heatmap among all scATAC-seq libraries (D).

(E–H) Quality control of snRNA-seq: distribution of total number of UMI (E); distribution of number of detected genes (F); distribution of the proportion of reads from organelle (G); and Spearman's correlation coefficient heatmap among all snRNA-seq libraries (H).

(I) Correlation of cell proportions between the first two replicates across scATAC-seq clusters for all tissues (Pearson's correlation coefficient: 0.98).

(J) Correlation of cell proportions between the two replicates across snRNA-seq clusters for all tissues (Pearson's correlation coefficient: 0.96).

(K and L) UMAP embeddings overlaid with cluster id for scATAC-seq (K) and snRNA-seq (L).

(M) *Z* score heatmap of Spearman's correlation coefficient across all laser-capture microdissection (LCM) RNA-seq datasets and scATAC-seq clusters.

(N) *Z* score heatmap of Spearman's correlation coefficient across LCM RNA-seq datasets and snRNA-seq clusters.

(O) UMAP embeddings for scATAC-seq overlaid predicted cluster ID in snRNA-seq.

(P) UMAP embeddings for snRNA-seq overlaid with raw cluster ID.

(Q) Frequency distribution of max prediction score of snATAC-seq nuclei from the TransferData function in Seurat.

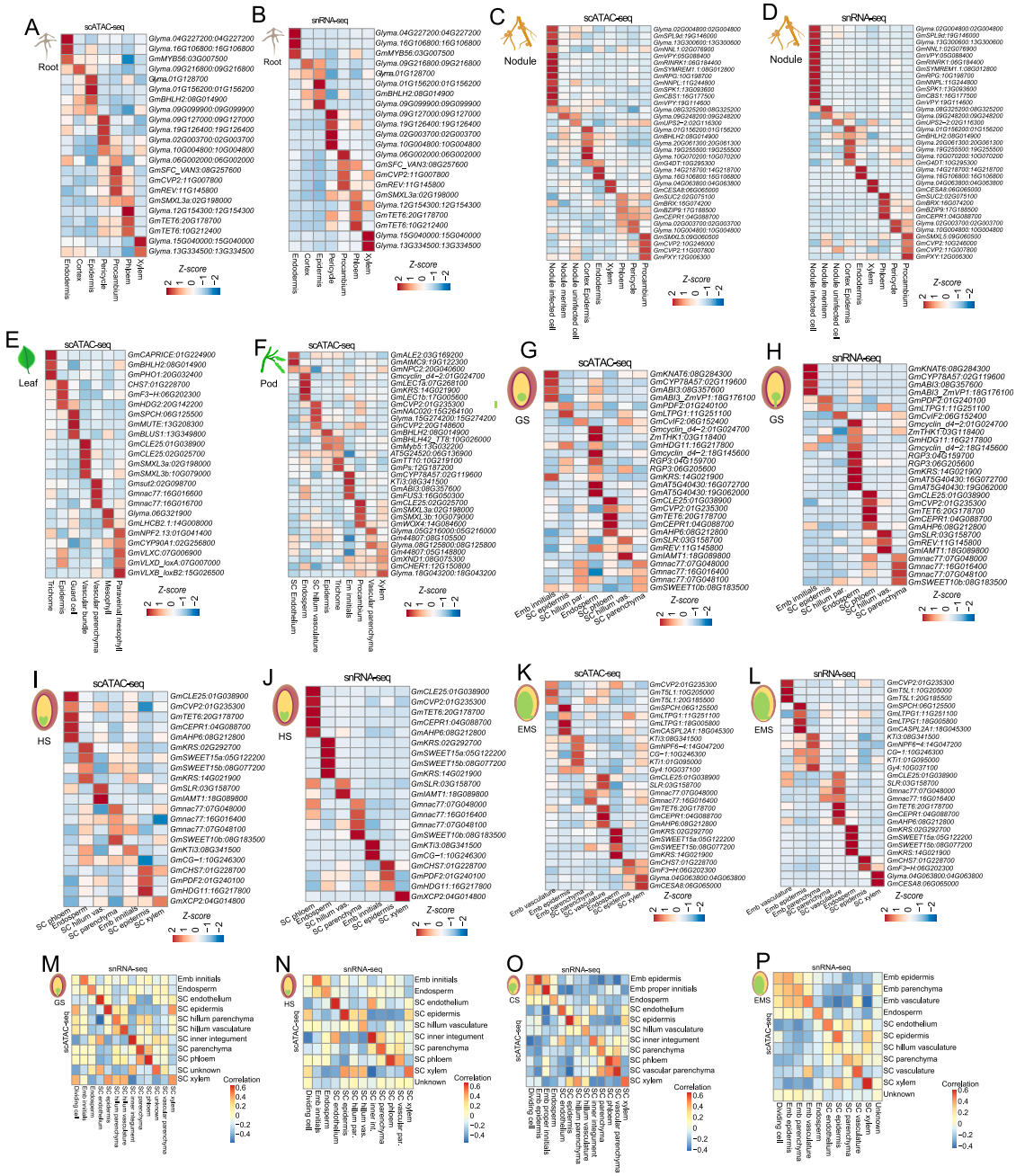

Figure S2. Marker-based annotation for scATAC-seq and snRNA-seq, related to Figure 1

(A and B) *Z* score heatmap of gene accessibility (A) and gene expression (B) for representative marker genes across shared cell types in soybean roots.

(C and D) *Z* score heatmap of gene accessibility (C) and gene expression (D) for representative marker genes across shared cell types in soybean nodules.

(E and F) *Z* score heatmap of gene accessibility for representative marker genes across cell types in soybean leaves (E) and pods (F).

(G and H) *Z* score heatmap of gene accessibility (G) and gene expression (H) for representative marker genes across shared cell types in soybean seeds at globular stage.

(I and J) *Z* score heatmap of gene accessibility (I) and gene expression (J) for representative marker genes across shared cell types in soybean seeds at heart stage.

(K and L) *Z* score heatmap of gene accessibility (K) and gene expression (L) for representative marker genes across shared cell types in soybean seeds at early maturation stage.

(M–P) The heatmap of Spearman's correlation coefficient between 1,000 most variable gene accessibility and expression across all cell types in each tissue, including seeds at globular stage (M), heart stage (N), cotyledon stage (O), and early maturation stage (P).

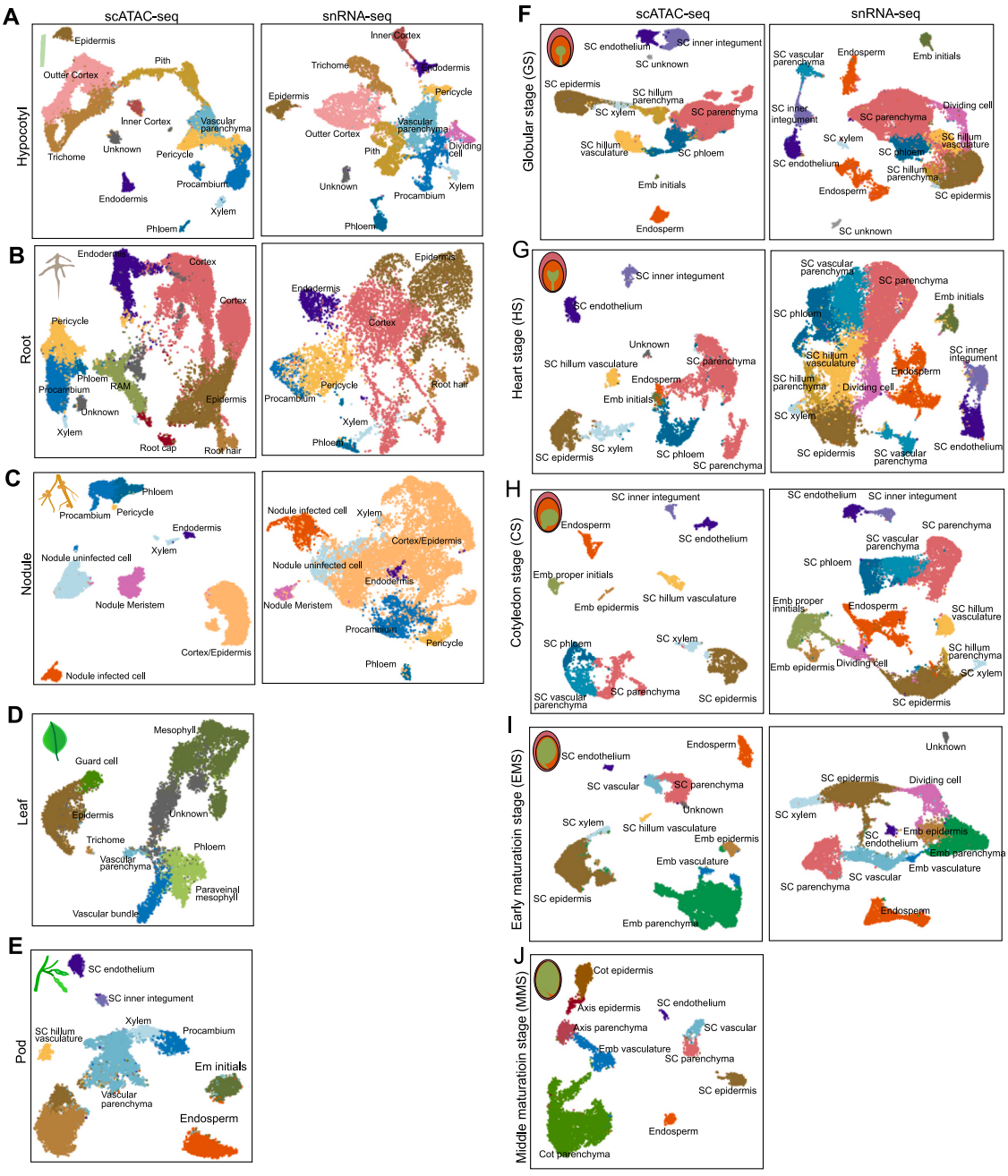

Figure S3. Cell-type annotation for nuclei from scATAC-seq and snRNA-seq, related to Figure 1

UMAP projection of nuclei, distinguished by assigned cell-type labels for scATAC-seq (left) snRNA-seq (right) across ten tissues, including hypocotyls (A), roots (B), nodules (C), leaves (D), pods (E), seeds at globular stage (F), heart stage (G), cotyledon stage (H), early maturation stage (I), and middle maturation stage (J).

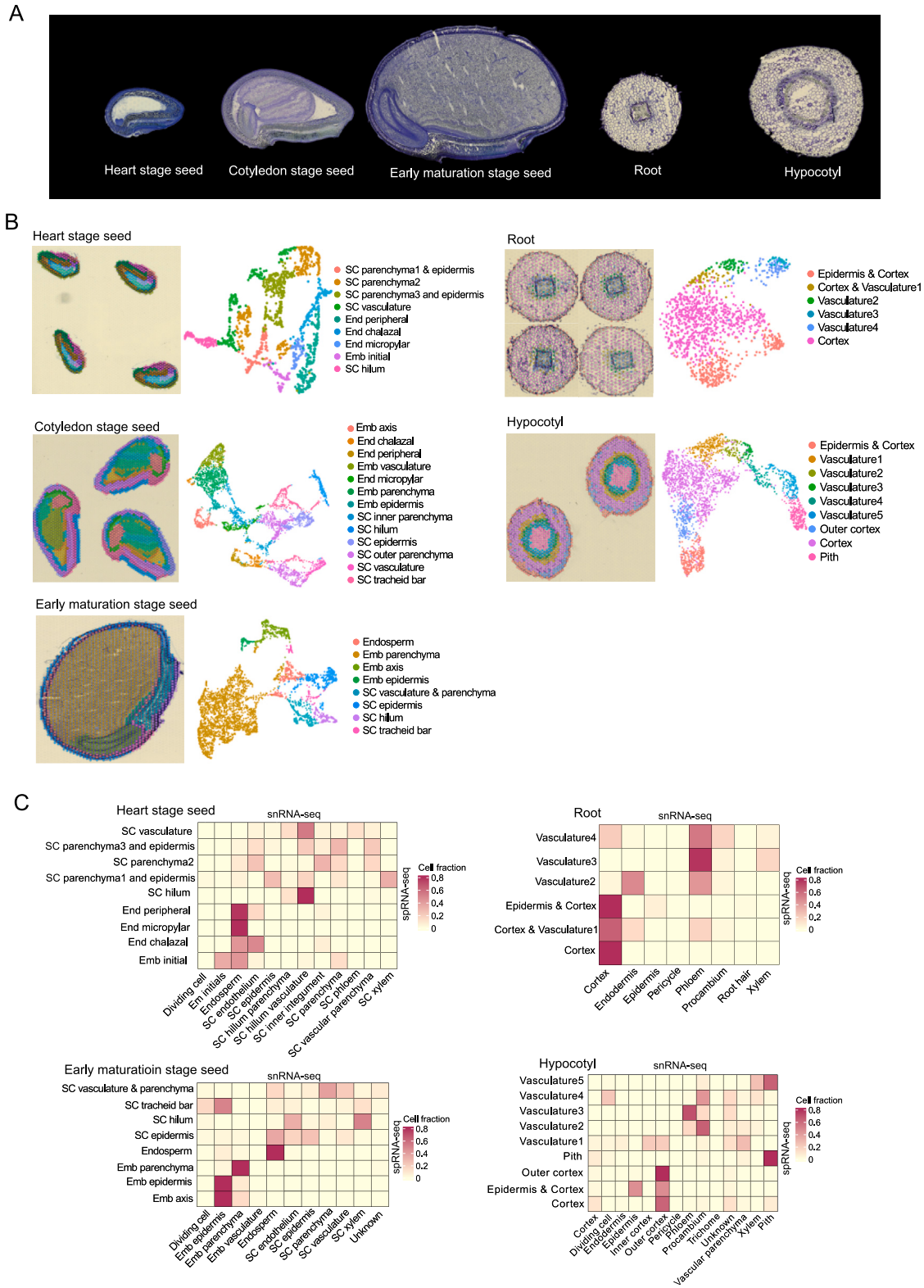

(legend on next page)

Figure S4. Spatial transcriptome atlas of soybean, related to Figure 2

(A) The histological structure of soybean tissues used for spRNA-seq.

(B) The visualization of spatial spot clusters on the tissue (left) and on the UMAP plot (right) for all the tissue types.

(C) Heatmaps of the snRNA-seq cell-type prediction scores on the spRNA-seq cell types for all the tissue types.

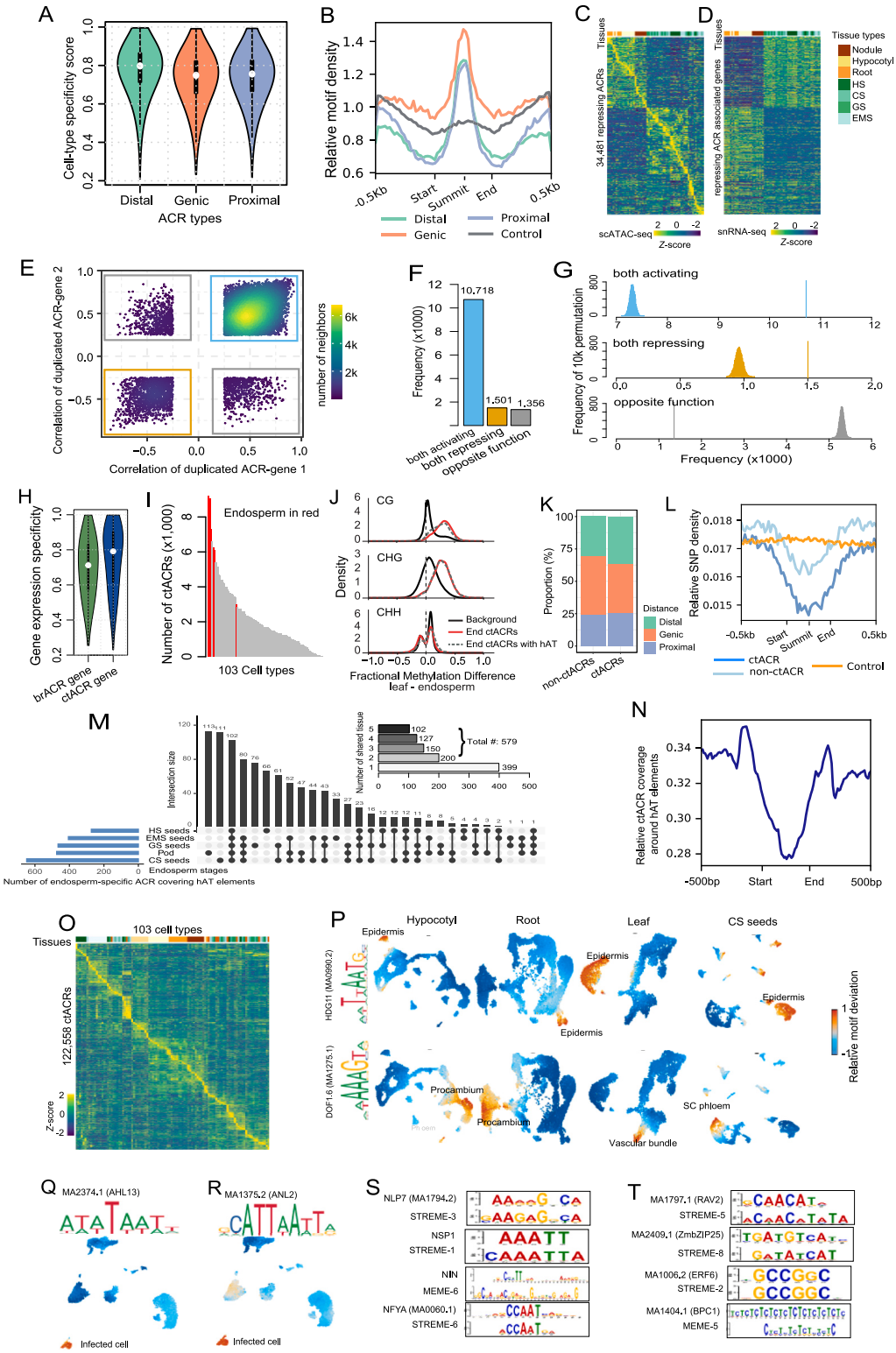

Figure S5. Characterization of ACRs and ctACRs, related to Figures 3 and 4

(A) Distribution of cell-type specificity score across three types of ACRs showing distal ACRs had significantly higher cell-type specificity than genic and proximal ACRs (t test, p value < $2.2e^{-16}$).

(B) Relative density within 500-bp flanking regions of different classes of ACRs and control regions.

(legend continued on next page)

(C and D) Heatmap showing chromatin accessibility of repressing ACRs (C) and the expression of associated genes (D).
(E) Comparison of ACR-gene correlations among duplicated regions.
(F) Bar plot of ACR-gene duplicate classifications.
(G) Permutation tests illustrating the null distributions of ACR-gene duplicate classification frequencies (histograms) compared with the observed frequencies (solid lines).
(H) Distribution of gene expression specificity scores for genes associated with broadly accessible chromatin regions (brACRs) and cell-type-specific ACRs (ctACRs).
(I) Distribution of number of ctACRs identified in each cell type. Endosperm cell types were highlighted in red.
(J) Frequency distribution of DNA methylation differences across 50-bp windows for (leaf − endosperm) across the genome (black lines), endosperm-specific ACRs (red lines), and endosperm-specific ACRs overlapping with hAT TEs (gray lines).
(K) Proportion of different groups of ACR in located in genic, proximal, and distal regions.
(L) Relative SNP density within 500-bp flanking regions of different groups of distal ACRs and control regions.
(M) UpSet plot showing the number of endosperm-specific ACRs covering hAT element across five tissues, including pod, globular stage seeds (GS seeds), heart stage seeds (HS seeds), cotyledon stage seeds (CS seeds), and early maturation stage seeds (EMS seeds).
(N) Average distribution of ctACR (n = 1,998) coverage around hAT elements.
(O) Heatmap showing relative chromatin accessibility of ctACR across 103 cell types.
(P) UMAP embeddings overlaid with motif deviation score of epidermis-specific TF HDG11 (top row) and vasculature-specific TF DOF1.6 (bottom row) across 4 tissues, including hypocotyl, root, leaf, and seeds at CS.
(Q and R) UMAP embeddings overlaid with motif deviation score of motif MA2374.1 (Q) and MA1375.2 (R) in nodule tissue.
(S) The motif sequence alignment of key nodulation-related TF motif (up) and *de novo* motif (bottom) enriched in infected-cell-specific ACRs.
(T) The motif sequence alignment of known TF motif in JASPAR2024 (up) and *de novo* motif (bottom) enriched in infected-cell-specific ACRs.

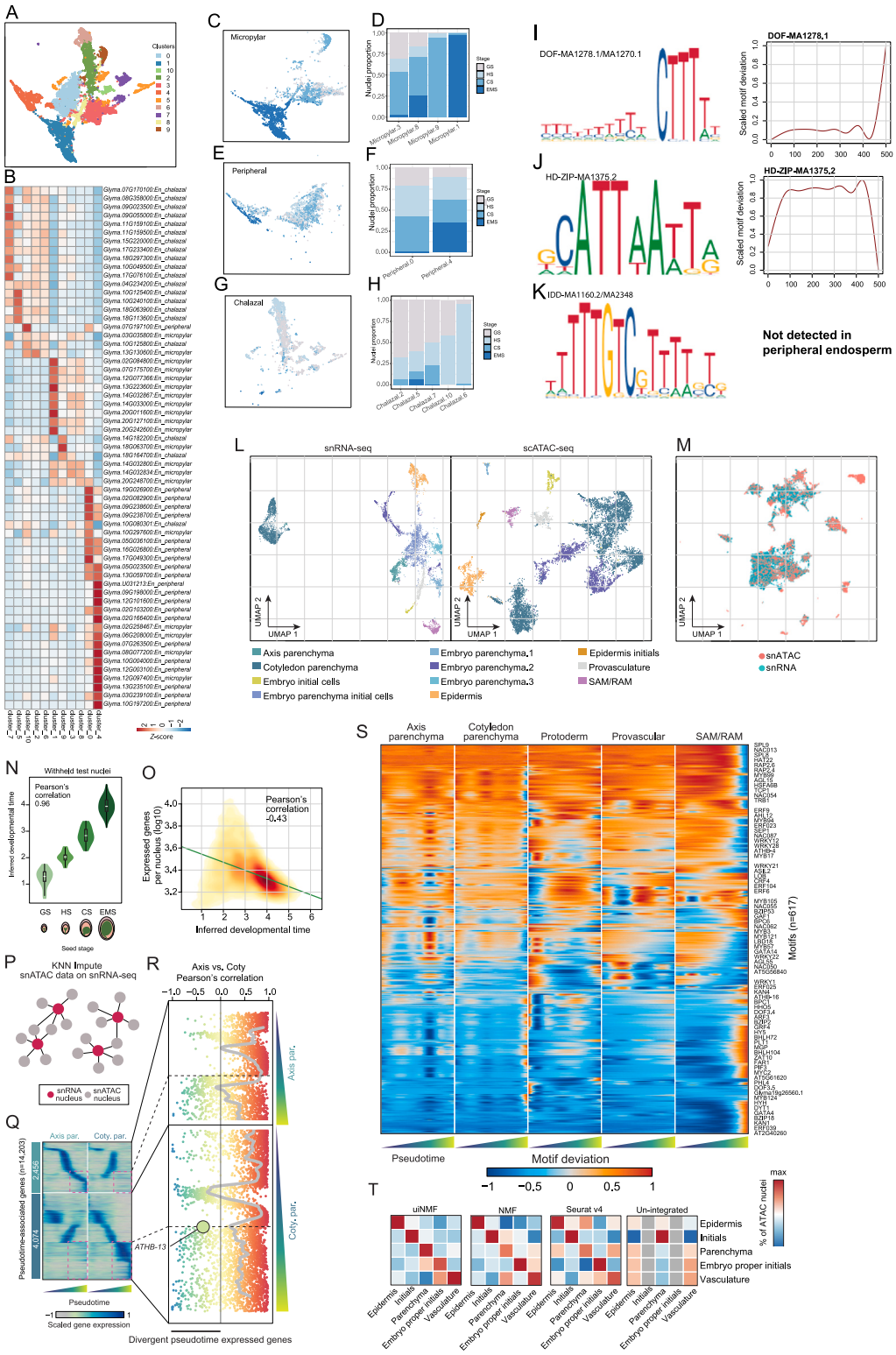

Figure S6. Analysis of three sub-cell types of endosperm and embryogenesis trajectories, related to Figures 5 and 6

(A) UMAP embeddings of integration of scATAC-seq and snRNA-seq for endosperm cells across 4 developmental stages, including globular stage, heart stage, cotyledon stage, and early maturation stage.

(legend continued on next page)

(B) *Z* score heatmap of gene expression for *de novo* marker genes for three sub-cell types of endosperm, including micropylar, peripheral, and chalazal endosperm from spRNA-seq of seeds at the cotyledon stage.
(C and D) UMAP embeddings of micropylar endosperm cells overlaid with four developmental stages (C) and nuclei proportion in four developmental stages across micropylar clusters (D): seed stages include GS, HS, CS, and EMS.
(E and F) Similar to (C and D), but for the peripheral endosperm.
(G and H) Similar to (C and D), but for the chalazal endosperm.
(I–K) The five motifs that were identified in ACRs of all the 13 SWEET transporter genes (left) and their motif deviation across peripheral endosperm developmental pseudotime (right).
(L) Cell-type annotation of snRNA-seq and scATAC-seq embryogenic nuclei.
(M) Integration of scATAC-seq and snRNA-seq embryo nuclei via non-negative matrix factorization.
(N) Comparison of inferred nuclei age derived from LASSO predictions across seed developmental stages from withheld test nuclei.
(O) Comparison of inferred nuclei age with the number of expressed genes (log_{10}).
(P) Illustration of scATAC-seq and snRNA-seq imputation strategy.
(Q) Gene expression dynamics across pseudotime for axis and cotyledon parenchyma trajectories. Red boxes highlight genes with divergent expression patterns.
(R) Correlation of gene expression profiles between axis and cotyledon parenchyma trajectories. ATHB-13 is highlighted.
(S) TF motif deviation scores across pseudotime for the five embryogenesis branches.
(T) Correspondence between the predicted cell-type label from snRNA-seq integration (columns) and marker-based cell-type label of the scATAC-seq nuclei (rows).

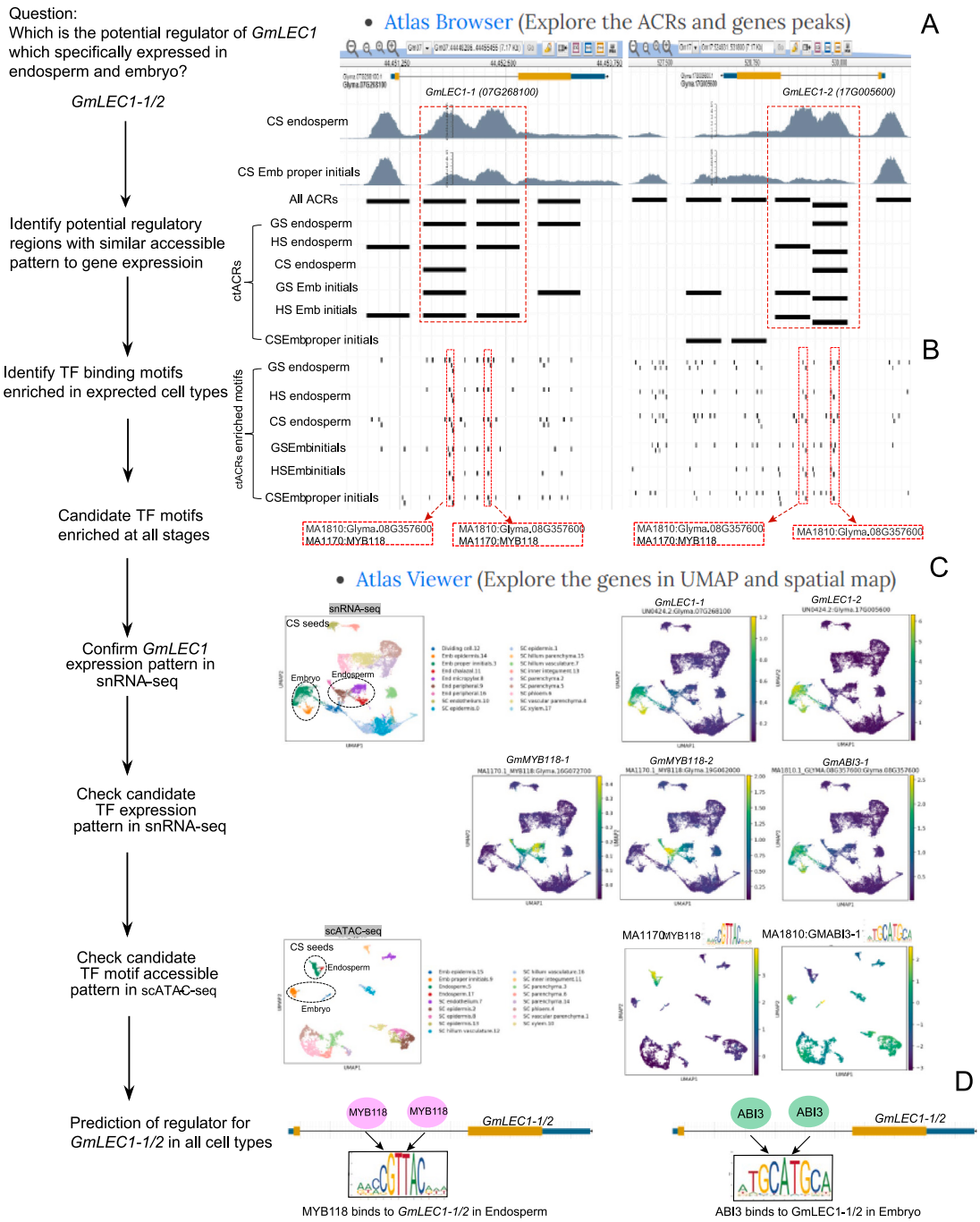

Figure S7. Workflow of exploring GmLEC1 genes regulatory network with soybean multi-omic atlas database, related to STAR Methods

(A) Two ACRs were identified in the first intron of the paralogs, which were specifically accessible in endosperm and embryo cells.

(B) These ACRs captured two motifs consistently enriched in endosperm or embryo cells at three stages of developing seeds: the GmABI3-1 (ABA INSENSITIVE3-1) motif, which controls embryo development and directly binds GmLEC1, and the MYB118 motif, which is specifically expressed in endosperm and control endosperm maturation in *Arabidopsis*.

(C) GmABI3-1 and its TF motif were mainly expressed and accessible, respectively, in embryo cells in CS seeds, while GmMYB118-1/2 and their TF motif were mainly expressed and accessible, respectively, in endosperm.

(D) We can propose a model where the specific use of the intronic MYB118 and ABI3 motifs contributes to the expression pattern of *GmLEC1-1/2*.